THE ASTROPHYSICAL JOURNAL, 565:696–719, 2002 February 1
© 2002. The American Astronomical Society. All rights reserved. Printed in U.S.A.

# MOLECULAR HYDROGEN, DEUTERIUM, AND METAL ABUNDANCES IN THE DAMPED Lyα SYSTEM AT $z_{abs} = 3.025$ TOWARD Q0347−3819[1]

SERGEI A. LEVSHAKOV,[2,3] MIROSLAVA DESSAUGES-ZAVADSKY,[4,5] SANDRO D'ODORICO,[4] AND PAOLO MOLARO[6]

*Received 2001 May 25; accepted 2001 October 4*

## ABSTRACT

We have detected in high-resolution spectra of the quasar Q0347−3819 obtained with the UV-Visual Echelle Spectrograph (UVES) at the VLT/Kueyen telescope over 80 absorption features in the Lyman and Werner $H_2$ bands at the redshift of a damped Lyα (DLA) system at $z_{abs} = 3.025$. At the same redshift, numerous absorption lines of atoms and low ions (H I, D I, C II, C II*, N I, O I, Si II, P II, Ar I, Cr II, Fe II, and Zn II) were identified. The $z_{abs} = 3.025$ system spans over $\sim 80$ km s$^{-1}$ and exhibits a multicomponent velocity structure in the metal lines. The main component at $z_{abs} = 3.024855$ shows a total $H_2$ column density $N(H_2) = (4.10 \pm 0.21) \times 10^{14}$ cm$^{-2}$ and a fractional molecular abundance $f_{H_2} = (1.94 \pm 0.10) \times 10^{-6}$ derived from the $H_2$ lines arising from the $J = 0$–5 rotational levels of the ground electronic vibrational state. In the second strong component at $z_{abs} = 3.024684$ we were able to set a stringent upper limit to $f_{H_2}$ of $3.3 \times 10^{-9}$ (3 $\sigma$ c.l.). The population of the $J$ levels can be represented by a single excitation temperature of $T_{ex} = 825 \pm 110$ K. The ortho-$H_2$:para-$H_2$ ratio equals $3.1 \pm 0.3$. This ratio is comparable to that calculated from hot $H_2$ formation upon grain surfaces (ortho-$H_2$:para-$H_2$ = 3:1) but is higher than the "freezeout" quantity (ortho-$H_2$:para-$H_2$ = 1:4) predicted for cosmological epochs at $z < 20$, implying recent formation of the hydrogen molecules following photodissociation of pristine $H_2$. In the main component the properties of the neutral atoms and low ions can be described with the same broadening parameter $b \simeq 3$ km s$^{-1}$ of the $H_2$ cloud. The rate at which UV photons are absorbed in the Lyman and Werner bands is found to be $\beta_0 \simeq 2 \times 10^{-9}$ s$^{-1}$. Taking into account that similar $\beta_0$ values are observed in the Galactic diffuse molecular clouds, it shows that the UV radiation fields in the DLA and in the Milky Way are very much alike. We also found the $H_2$ formation rate of $Rn_H \simeq 3 \times 10^{-16}$ s$^{-1}$ at $z_{abs} = 3.025$, which is consistent with observations in the Galactic disk diffuse clouds where $n_{H_2}$ is low. Comparing the relative rotational population ratios of $H_2$ with the measured C II*/C II ratio, we can infer that $n_H \simeq 6$ cm$^{-3}$ in the main component, which gives a size of $D \simeq 14$ pc along the line of sight. The mean value of the dust-to-gas ratio estimated for the whole $z_{abs} = 3.025$ system from the [Cr/Zn] ratio is equal to $\tilde{k} = 0.032 \pm 0.005$ (in units of the mean Galactic interstellar medium value). For the first time we unambiguously reveal a pronounced [α-element/iron peak] enhancement of [O, Si/Zn] $= 0.6 \pm 0.1$ (1 $\sigma$ c.l.) at high redshift. The simultaneous analysis of metal and hydrogen lines leads to D/H $= (3.75 \pm 0.25) \times 10^{-5}$. This value is consistent with standard big bang nucleosynthesis if the baryon-to-photon ratio, $\eta$, lies within the range $4.37 \times 10^{-10} \lesssim \eta \lesssim 5.32 \times 10^{-10}$, implying $0.016 \lesssim \Omega_b h_{100}^2 \lesssim 0.020$.

*Subject headings:* cosmology: observations — intergalactic medium — quasars: absorption lines — quasars: individual (Q0347−3819)

## 1. INTRODUCTION

Molecular hydrogen $H_2$, being the most abundant molecular species in the universe, plays a central role in star formation processes both at low and high redshifts (e.g., Shull & Beckwith 1982). The $H_2$ molecule is known to be an important coolant for gravitational collapse of hydrogen clouds at $T \sim 1000$ K. Fractional abundances of $H_2$ in interstellar H I regions were calculated first by Gould & Salpeter (1963) and by Hollenbach, Werner, & Salpeter (1971). They predicted the fractional abundance of molecular hydrogen $f_{H_2} \simeq 10^{-3}$, where $f_{H_2} = 2n_{H_2}/(n_H + 2n_{H_2})$ for a standard Galactic disk cloud with $n_H \simeq 10$ cm$^{-3}$, gas temperature of about 100 K, and the optical depth to the cloud center due to dust grains $\tau_g \simeq 0.1$.

The first detection of $H_2$ in the interstellar medium (ISM) was performed by Carruthers (1970) with a rocket-borne ultraviolet spectrometer. Later, after the launch of the *Copernicus* satellite, the far-UV absorption bands of $H_2$ were observed in the Galactic disk toward numerous relatively bright stars with visual extinctions $A_V$ of less than about 1 mag (e.g., Spitzer & Jenkins 1975; Savage et al. 1977). More recent observations of $H_2$ with the interstellar medium absorption profile spectrograph (IMAPS) (Jenkins & Peimbert 1997), the *Orbiting and Retrievable Far and Extreme Ultraviolet Spectrometer* (*ORFEUS*) (Richter et al. 1998; de Boer et al. 1998), and the *Far Ultraviolet Spectroscopic Explorer* (*FUSE*) (Moos et al. 2000) have shown the ubiquity of $H_2$ in the disk and halo of the Galaxy and in the

[1] Based on public data released from UVES Commissioning at the VLT Kueyen telescope, ESO, Paranal, Chile.

[2] Division of Theoretical Astrophysics, National Astronomical Observatory, Tokyo 181-8588, Japan; lev@th.nao.ac.jp.

[3] Department of Theoretical Astrophysics, Ioffe Physico-Technical Institute, St. Petersburg 194021, Russia; lev@astro.ioffe.rssi.ru.

[4] European Southern Observatory, Karl-Schwarzschild-Strasse 2, D-85748 Garching bei München, Germany; sdodoric@eso.org.

[5] Observatoire de Genève, CH-1290 Sauverny, Switzerland; mdessaug@eso.org.

[6] Osservatorio Astronomico di Trieste, via G.B. Tiepolo 11, I-34131 Trieste, Italy; molaro@oat.ts.astro.it.

Magellanic Clouds. In the *FUSE* minisurvey, $H_2$ was detected in the sight lines with neutral hydrogen column densities $N(\text{H I}) \simeq (3\text{–}6) \times 10^{20}$ cm$^{-2}$, the fractional abundances $f_{H_2} \simeq 7.4 \times 10^{-6}$ to $3.4 \times 10^{-2}$, and the excitation temperatures $T_{ex} \simeq 180$–540 K (Shull et al. 2000).

In these observations the range of $N(\text{H I})$ resembles the range of hydrogen column densities measured in QSO damped Ly$\alpha$ (DLA) systems, the systems with $N(\text{H I}) > 2 \times 10^{20}$ cm$^{-2}$, which are believed to originate in intervening galaxies or protogalaxies located at cosmological distances (Wolfe et al. 1995). Thus, we may expect to observe far-UV $H_2$ lines from electronic vibrational rotational bands shifted to the blue spectral range ($\lambda > 3000$ Å) at $z \gtrsim 2$. The detection of the first $H_2$-bearing cosmological cloud in the $z_{abs} = 2.811$ DLA system toward Q0528−250 was made by Levshakov & Varshalovich (1985) and later confirmed by Foltz, Chaffee, & Black (1988). Two additional $H_2$ systems were found at $z_{abs} = 1.97$ toward Q0013−004 (Ge & Bechtold 1997) and at $z_{abs} = 2.34$ toward Q1232+0815 (Ge & Bechtold 1999). The latter was recently confirmed by Petitjean, Srianand, & Ledoux (2000). The fourth identification of $H_2$ was made at $z_{abs} = 3.39$ toward Q0000−2620 by Levshakov et al. (2000b, 2001), and a tentative fifth $H_2$ system was reported by Petitjean et al. (2000) at $z_{abs} = 2.374$ toward Q0841+129.

Molecular gas in the early universe has also been detected through the spectral line emission from the tracer carbon monoxide (CO) molecule in the ultraluminous galaxy IRAS 10215+4724 at $z = 2.28$ (Brown & vanden Bout 1992; Solomon, Downes, & Radfort 1992), in the cloverleaf quasar H1413+117 at $z = 2.56$ (Barvainis et al. 1997), in the quasar BR 1202−0725 at $z = 4.69$ (Ohta et al. 1996; Omont et al. 1996), in the quasar BRI 1335−0418 at $z = 4.41$ (Guilloteau et al. 1997; Carilli, Menten, & Yun 1999), in the IR luminous galaxy J14011+0252 at $z = 2.565$ (Frayer et al. 1999), in the extremely red galaxy HR 10 at $z = 1.44$ (Andreani et al. 2000), in two powerful radio galaxies 4C 60.07 and 6C 1909+722 at $z = 3.79$ and 3.53, respectively (Papadopoulos et al. 2000), in the lensed quasar APM 08279+5255 at $z = 3.911$ (Downes et al. 1999; Papadopoulos et al. 2001), and in the QSO SDSS 1044−0125 at $z = 5.8$ (Iwata et al. 2001).

However, identification of $H_2$ lines in the DLA systems remains a rather rare event. Most DLA systems yielded only upper limits of $f_{H_2} \lesssim 10^{-7}$ to $10^{-6}$. The lack of $H_2$ in these systems might be a consequence of the lower metal abundances, lower dust contents, and higher temperature and ultraviolet fluxes when compared with the ISM in the Galaxy and in the Magellanic Clouds. Low molecular abundances found in high-redshift DLA systems resemble the properties of, at least, one local DLA system: the metal-deficient ($Z/Z_\odot \sim 1/50$) starburst blue compact galaxy I Zw 18 with $N(\text{H I}) \simeq 3 \times 10^{21}$ cm$^{-2}$ (Kunth et al. 1994) where recent *FUSE* observations set a limit of $f_{H_2} \ll 10^{-6}$(Vidal-Madjar et al. 2000).

The measured upper limits of $f_{H_2}$ in high-redshift metal-poor DLA systems are slightly lower than the calculated fraction of molecules in the pristine gas: $f_{H_2} \simeq 10^{-6}$ to $10^{-5}$ depending on cosmological models (e.g., Galli & Palla 1998). Although UV photons produced by the first objects can quickly destroy all $H_2$ in the pristine gas and thus delay further structure formation (Haiman, Rees, & Loeb 1997), we may expect that the electrons in the photoionized regions around first stars will in turn act as a catalyst in the $H^-$ channel to produce $H_2$ at redshifts $z < 50$ where the $H^-$ channel proceeds much more quickly than the $H^+$ one (Fuller & Couchman 2000). Therefore, direct measurements of gas density, UV radiation field, and $H_2$ formation and destruction rates in DLA systems may shed light on star formation processes at very high redshift.

In this paper we present results of the study of $H_2$ lines identified in the sixth DLA system at $z_{abs} = 3.025$ toward Q0347−3819. We also use the information from the molecular lines together with H and metal lines to refine the deuterium abundance determination by D'Odorico, Dessauges-Zavadsky, & Molaro (2001, hereafter DDM01) and the values of metal abundances (DDM01; Prochaska & Wolfe 1999).

The outline of the paper is as follows. We discuss observations in § 2. The methods of data analysis are presented in § 3. The identification of $H_2$ lines and the calculation of their proper redshift is given in § 3.1. The broadening parameter $b$ is evaluated in § 3.2. The column densities $N(J)$ for the rotational levels from $J = 0$ to 5 of the lowest vibrational level $v = 0$ in the ground electronic state $X^1\Sigma_g^+$ (for the $H_2$ notation see Field, Sommerville, & Dressler 1966), the fractional molecular abundance, and the ortho-$H_2$:para-$H_2$ ratios are calculated in § 3.3. In § 3.4 we compute the excitation temperature $T_{ex}$. The results of a stacking technique applied to the measurements of the abundances of Zn II and Cr II ions and the dust-to-gas ratio in the whole $z_{abs} = 3.025$ system are estimated in § 3.5. In § 3.6 we analyze within one self-consistent model all available profiles of H, D, neutral atoms, and low ions to infer column densities and relative abundances of D/H and metals. In § 4 we discuss the results and present their further analysis. In § 4.1 we estimate the kinetic temperature, $T_{kin}$, and the gas volumetric density, $n_H$, using the C II*/C II and C I/C II ratios. The distribution of $H_2$ over the rotational levels, the photodissociation rate of $H_2$, and the rate of the molecular hydrogen formation upon grain surfaces are considered in § 4.2. The revealed [$\alpha$-element/iron peak] enhancement is discussed in § 4.3. In § 5 we summarize the results.

## 2. OBSERVATIONS

Q0347−3819 is a bright quasar ($V = 17.3$) with $z_{em} = 3.23$ discovered by Osmer & Smith (1980), which shows a DLA system at $z_{abs} = 3.0245$. A column density of $N(\text{H I}) = (6.3^{+1.6}_{-1.3}) \times 10^{20}$ cm$^{-2}$ was first measured by Williger et al. (1989) and later confirmed by Pettini et al. (1994) as $N(\text{H I}) = (5 \pm 1) \times 10^{20}$ cm$^{-2}$. Q0347−3919 has a rich absorption-line spectrum studied by Pierre, Shaver, & Robertson (1990), Centurión et al. (1998), Ledoux et al. (1998), and Prochaska & Wolfe (1999).

High-quality data of this QSO in the UV ($3650 < \lambda < 4900$ Å) and in the near-IR ($6700 < \lambda < 10000$ Å) ranges were obtained during the commissioning of the UV-Visual Echelle Spectrograph (UVES) on the VLT 8.2 m Kueyen telescope at Paranal, Chile, in 1999 December and have been released for public use. UVES is described by D'Odorico et al. (2000) and details of the data reduction are given in Ballester et al. (2000). Two exposures of 4500 and 5000 s, covering the UV and the near-IR ranges, were obtained with a resolution FWHM $\simeq 7.0$ and $\simeq 5.7$ km s$^{-1}$, respectively. An average signal-to-noise ratio (S/N) per pixel of $\sim$20, 25, 40, and 15 was achieved in the final spectrum at $\lambda \sim 3650$, 4900, 6700, and 10000 Å, respectively.

The $z_{abs} = 3.025$ DLA exhibits a multicomponent velocity structure with the dominating component at $z_{abs} = 3.024856$ as found by DDM01, who discussed the first detection of the deuterium lines in DLA systems. The total H I column density derived in DDM01 from the best fit of Ly$\beta$ equals $(4.3 \pm 1.0) \times 10^{20}$ cm$^{-2}$, which agrees well with the measurement of Pettini et al. (1994) from Ly$\alpha$. The ionization structure of this DLA is also complex. There are at least two gas components: a warm gas seen in lines of neutral atoms, $H_2$, and low ions, and a hot gas where the resonance doublets of C IV and Si IV are formed. These high-ion transitions, observed by Prochaska & Wolfe (1999) with the Keck High Resolution Echelle Spectrometer (HIRES), show, however, different profile shapes as compared with the low-ion transitions. The physical properties of the hot gas component will not be studied in the present paper.

## 3. MEASUREMENTS

All absorption lines studied in the present paper lie in the Ly$\alpha$ forest where their analysis is complicated by possible H I contaminations and uncertainties in a local continuum, drawn by using "continuum windows" in the Ly$\alpha$ forest which could be located quite far from the feature under analysis. This kind of uncertainty is illustrated in Figure 1, where a portion of the Q0347−3819 spectrum with a few identified $H_2$ lines is shown. To achieve the highest possible accuracy under these circumstances, we have always used in parallel several different lines to derive the physical parameters of the DLA system.

### 3.1. *Redshift of the* $H_2$ *System*

Wavelengths, oscillator strengths, and radiation damping constants for the Lyman and Werner bands of the $H_2$ molecule were taken from the theoretical calculations of Abgrall & Roueff (1989). These data seem to be reasonably accurate as shown by high spectral resolution IMAPS measurements of molecular hydrogen toward the Orion belt stars (Jenkins et al. 2000).

The identification of the $H_2$ lines was started from the subsystem which has the largest H I column density (see § 3.6). Preliminary inspection of the Q0347−3819 spectrum revealed 88 absorption features at the expected positions of the $H_2$ lines. However, not all of them were suitable for further analysis because of H I contaminations. For this reason, to estimate $z_{H_2}$ we used only those $H_2$ lines which show symmetric profiles with their blue and red sides reaching the continuum. These lines are listed in Table 1.

Given a fit to the continuum and the line measurement interval, the equivalent width $W_\lambda$, the line center $\langle\lambda\rangle$, and their errors $\sigma_{W_\lambda}$ and $\sigma_{\langle\lambda\rangle}$ can be computed from the following equations (e.g., Levshakov et al. 1992):

$$W_\lambda = \Delta\lambda \sum_{i=1}^{M} (1 - F_i) , \tag{1}$$

$$\langle\lambda\rangle = \frac{\Delta\lambda}{W_\lambda} \sum_{i=1}^{M} \lambda_i (1 - F_i) , \tag{2}$$

$$\sigma_{W_\lambda} = \Delta\lambda \left[ \sum_{i=1}^{M} \sigma_i^2 + \left\langle \frac{\sigma_c}{C} \right\rangle^2 (M - W')^2 \right]^{1/2} , \tag{3}$$

and

$$\sigma_{\langle\lambda\rangle} = \left[ \frac{\Delta\lambda}{W_\lambda} \sum_{i=1}^{M} (\lambda_i - \langle\lambda\rangle)^2 (1 - F_i) \right]^{1/2} , \tag{4}$$

where $\Delta\lambda$ is the wavelength interval between pixels, $M$ is the number of pixels involved in the sum, $F_i$ is the normalized intensity in the $i$th pixel whose wavelength is $\lambda_i$, $\sigma_i$ is the noise level in the $i$th pixel, $W' = W_\lambda/\Delta\lambda$ is the dimensionless equivalent width in pixels, and $\langle\sigma_c/C\rangle$ is the mean accuracy of the continuum fit over the line measurement interval.

The errors in $W_\lambda$ and $\langle\lambda\rangle$ are caused mainly by the finite number of photons counted. In addition, for weak absorption features ($W' \ll 1$) the second term in equation (3) is of about the same order of magnitude as the first one, meaning that the identification of weak $H_2$ lines is very sensitive to the accuracy of the local continuum fitting.

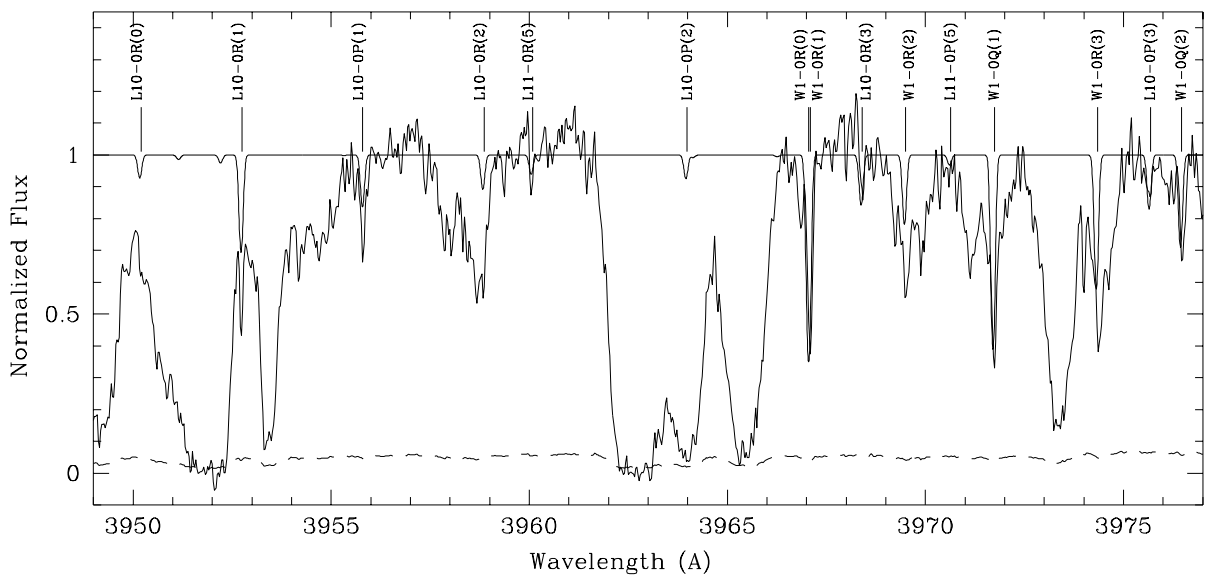


FIG. 1.—Portion of the normalized spectrum of Q0347−3819 in the region of a few $H_2$ lines from the Lyman and Werner bands (labels "L" and "W," respectively) identified in the $z_{abs} = 3.025$ DLA system. The noise level is indicated by the dashed curve at the bottom of the panel. The general continuum was estimated by using a polynomial fit to the "continuum windows" in all spectral ranges spanning about 1200 Å. In cases in which the curvature of the QSO continuum at $z = 3.025$ is strong, the uncertainty in the local continuum level may be dominated by uncertainties in the fitting procedure.

TABLE 1

$H_2$ LINES AT $z_{abs} = 3.025$ TOWARD Q0347−3819

| $J$ (1) | Line (2) | $\langle\lambda\rangle$ (Å) (3) | $\sigma_{\langle\lambda\rangle}$ (Å) (4) | $W_\lambda$ (mÅ) (5) | $\sigma_{W_\lambda}$ (mÅ) (6) | $z$ (7) | $\sigma_z$ (8) |
|---|---|---|---|---|---|---|---|
| 0..... | L3-0R[a] | 4277.96 | 0.09 | 6.7 | 4.4 | 3.02486 | 0.00009 |
| | L7-0R[a,b] | 4076.44 | 0.06 | 25.8 | 5.7 | 3.02485 | 0.00006 |
| 1..... | W2-0Q[b] | 3888.38 | 0.03 | 83.9 | 4.4 | 3.02487 | 0.00003 |
| | W3-0Q[b] | 3813.22 | 0.05 | 55.7 | 7.2 | 3.02484 | 0.00005 |
| | L1-0P[b] | 4403.42 | 0.04 | 25.4 | 4.1 | 3.02486 | 0.00004 |
| | L3-0R[b] | 4280.27 | 0.03 | 65.6 | 3.8 | 3.02485 | 0.00002 |
| | L3-0P[a,b] | 4284.89 | 0.04 | 24.2 | 4.2 | 3.02486 | 0.00004 |
| | L7-0R[b] | 4078.95 | 0.03 | 76.4 | 4.8 | 3.02485 | 0.00003 |
| | L10-0P[b] | 3955.77 | 0.04 | 46.8 | 5.0 | 3.02484 | 0.00004 |
| | L14-0P[a,b] | 3813.61 | 0.09 | 24.6 | 7.2 | 3.02484 | 0.00009 |
| 2..... | W0-0R[a,b] | 4061.19 | 0.05 | 34.4 | 5.5 | 3.02488 | 0.00005 |
| | W0-0Q[a,b] | 4068.87 | 0.04 | 50.7 | 6.7 | 3.02484 | 0.00004 |
| | W0-0P[b] | 4073.85 | 0.09 | 10.3 | 4.1 | 3.02488 | 0.00009 |
| | W1-0Q[b] | 3976.45 | 0.04 | 36.6 | 4.4 | 3.02487 | 0.00004 |
| | L3-0R[a,b] | 4286.44 | 0.06 | 14.9 | 4.7 | 3.02485 | 0.00006 |
| | L3-0P[b] | 4294.12 | 0.07 | 12.6 | 3.9 | 3.02485 | 0.00007 |
| | L4-0R[a,b] | 4232.14 | 0.05 | 24.9 | 5.0 | 3.02487 | 0.00005 |
| | L5-0R[a,b] | 4180.57 | 0.04 | 32.2 | 4.4 | 3.02485 | 0.00004 |
| 3..... | W0-0Q[b] | 4075.88 | 0.03 | 65.7 | 5.0 | 3.02485 | 0.00003 |
| | L2-0R[b] | 4353.77 | 0.03 | 36.1 | 4.6 | 3.02488 | 0.00003 |
| | L2-0P[a] | 4365.17 | 0.07 | 8.6 | 5.7 | 3.02481 | 0.00007 |
| | L3-0R[b] | 4296.43 | 0.03 | 51.4 | 4.6 | 3.02484 | 0.00003 |
| | L3-0P[a,b] | 4307.18 | 0.05 | 22.0 | 4.5 | 3.02487 | 0.00005 |
| | L4-0R[b] | 4252.15 | 0.03 | 61.1 | 5.4 | 3.02486 | 0.00003 |
| | L4-0P[a] | 4252.14 | 0.09 | 8.4 | 6.0 | 3.02486 | 0.00008 |
| | L6-0R[b] | 4141.54 | 0.03 | 60.3 | 4.6 | 3.02487 | 0.00003 |
| | L7-0P[b] | 4103.35 | 0.05 | 32.2 | 4.0 | 3.02484 | 0.00005 |
| | L8-0P[a,b] | 4058.61 | 0.05 | 30.1 | 5.5 | 3.02484 | 0.00005 |
| | L12-0R[a,b] | 3894.77 | 0.04 | 49.0 | 6.2 | 3.02488 | 0.00005 |
| | L15-0R[a,b] | 3795.31 | 0.08 | 20.8 | 5.0 | 3.02486 | 0.00008 |
| 4..... | L4-0P[a,b] | 4268.64 | 0.05 | 24.1 | 5.9 | 3.02482 | 0.00005 |
| | L8-0P[a] | 4074.21 | 0.09 | 8.6 | 5.0 | 3.02484 | 0.00009 |
| 5..... | W1-0Q[a,b] | 4004.44 | 0.06 | 25.7 | 5.4 | 3.02489 | 0.00006 |
| | L7-0P[a,b] | 4138.55 | 0.10 | 8.5 | 4.7 | 3.02484 | 0.00010 |
| | L12-0R[a,b] | 3923.76 | 0.08 | 13.9 | 4.4 | 3.02484 | 0.00008 |

[a] Lines are used in the Voigt fitting procedure to estimate the broadening parameter $b$.

[b] Lines are used in Fig. 3.

The analyzed 35 transitions of the Lyman and Werner bands are listed in column (2) of Table 1, whereas their $J$-values are given in column (1). The measured heliocentric position of the center of each spectral feature and its standard deviation were calculated according to equations (2) and (4) and are presented in columns (3) and (4), respectively. The observed equivalent widths (col. [5]) and their errors (col. [6]) were calculated according to equations (1) and (3). Note that the rest-frame equivalent width equals $W_{\lambda,\mathrm{rest}} = W_\lambda/(1 + z_{H_2})$. In these calculations we set for all lines $\langle\sigma_c/C\rangle = 1\%$ to account for the uncertainty in the local continuum level. A formal mean value of $\langle\sigma_c/C\rangle$ estimated from the continuum windows is less than or about 1%. In particular, $\langle\sigma_c/C\rangle = 0.70\%$ for L3-0R(0) and 1.03% for L7-0P(5), which are shown in the figures listed in § 3.3. Column (7) lists the measured redshifts for each $H_2$ transition, while their errors $|\sigma_z| = |\sigma_{\langle\lambda\rangle}|/\lambda_0$ (where $\lambda_0$ is the rest-frame wavelength from Abgrall & Roueff 1989) are shown in column (8). The weighted mean redshift yields $z_{H_2} = 3.024855 \pm 0.000005$, which coincides exactly with the redshift of the strongest main component in metal line profiles given by DDM01. Thus, at a given S/N and spectral resolution we do not find any systematic shifts larger than a few kilometers per second in the radial velocities between neutral atoms and $H_2$ molecules in the molecular cloud at $z_{abs} = 3.025$.

Previous *Copernicus* investigations of diffuse gas in the Galaxy showed that the mean radial velocity of $H_2$ lines differs from the corresponding mean of the atomic lines. For instance, the differences of $\Delta v \simeq 5$ km s$^{-1}$ toward $\lambda$ Sco (Spitzer & Jenkins 1975) and $\Delta v \simeq 11$ and $\simeq 6$ km s$^{-1}$ toward, respectively, $\tau$ Sco and $\zeta$ Oph (Spitzer, Cochran, & Hirshfeld 1974) were detected. At the UVES spectral resolution such differences, in case they were present, could be easily distinguished.

### 3.2. *Line Broadening*

The measurement of the broadening parameter $b$[7] and the calculation of the confidence ranges for its mean value were carried out in two steps. First, a least-squares analysis was applied to the line fitting. We combined 17 $H_2$ lines

[7] By definition $b = \sqrt{2}\sigma_v$, where $\sigma_v$ is the one-dimensional Gaussian velocity dispersion of molecules along the line of sight.

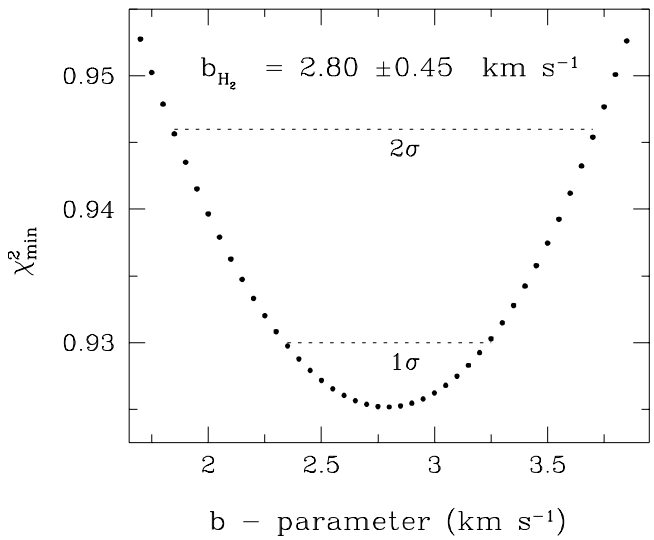


FIG. 2.—Confidence regions in the "$\chi^2$-$b$" plane calculated from the simultaneous fit of the $H_2$ lines from Table 1 as described in the text. The parabola vertex corresponds to the most probable value of $b = 2.80$ km s$^{-1}$.

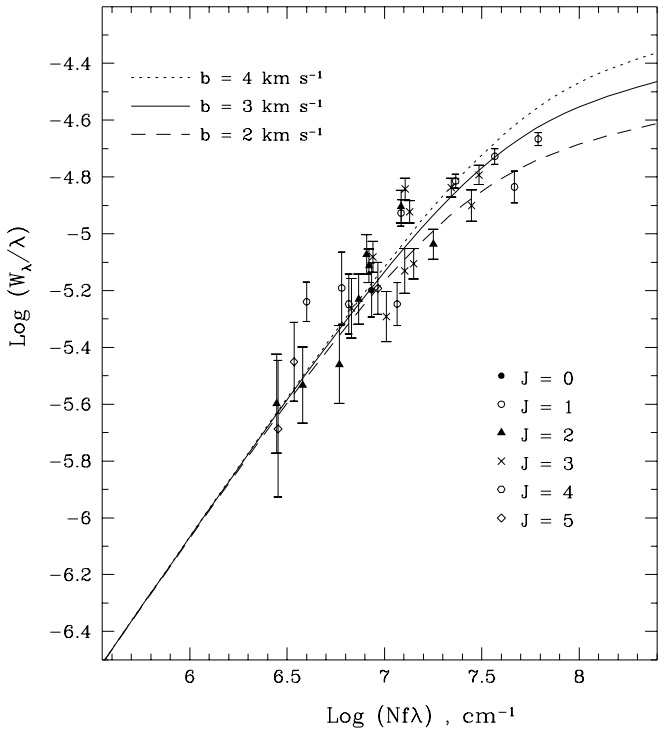


FIG. 3.—Curves of growth for 31 $H_2$ lines ($J = 0$, 1, 2, 3, 4, and 5; see Table 1) in the $z_{abs} = 3.025$ molecular cloud toward Q0347−3819. The most probable Doppler parameter is $b_{H_2} = 3$ km s$^{-1}$. Curves with $b = 2$ and 4 km s$^{-1}$ restrict the 1 $\sigma$ confidence region for $b_{H_2}$.

(L3-0R0, L7-0R0, W3-0Q1, L3-0P1, W0-0R2, W0-0Q2, L3-0R2, L4-0R2, L2-0P3, L2-0R3, L4-0R3, L4-0P3, L8-0P3, L12-0R3, L4-0P4, L8-0P4, W1-0Q5) from Table 1 and fitted them simultaneously with the individual Gaussian profiles. These lines were chosen because they exhibit "clean," uncontaminated profiles. The $H_2$ line centers were fixed at the mean $z_{H_2}$, and the theoretical profiles were convolved with the instrumental point-spread function (PSF), which was approximated by a Gaussian with FWHM = 7.0 km s$^{-1}$, i.e., $b_{PSF} = 4.2$ km s$^{-1}$. The $\Delta\chi^2$ method (Press et al. 1992) was used to estimate the most probable $b$-value and its error.[8] For a given current value of $b$ taken from the range ($b_{min}$, $b_{max}$), we minimized $\chi^2$ (normalized per degree of freedom) by varying the line intensities independently (we consider $\chi^2_{min}$ as a $\chi^2$ distribution with $\nu = \mathcal{N} - \mathcal{M}$ degrees of freedom, where the number of data points $\mathcal{N} = 192$ and the number of fitted parameters $\mathcal{M} = 6$ for this particular case). With this we tried to check possible H I contaminations: the optimization procedure would fail to reach $\chi^2_{min} \simeq 1$ if the chosen $H_2$ lines were essentially contaminated by the Ly$\alpha$ forest absorption. The calculated $\chi^2_{min}$-values in dependence of $b$ and the 1 and 2 $\sigma$ confidence levels are shown in Figure 2. With $\chi^2_{min} = 0.925$ the most likely value for $b_{H_2}$ was found to be $2.80 \pm 0.45$ km s$^{-1}$ (s.d.).

In the second step, to check the obtained value and to infer the Doppler parameter independently, we calculated an optimal curve of growth for the $H_2$ lines from Table 1. The curve is shown by the solid line in Figure 3. In principle, it cannot be excluded that some unknown absorption lines blend with $H_2$ features, despite their symmetric and undisturbed profiles. Thus, the scatter of points in Figure 3 can be explained by this effect as well as by errors remaining after the continuum fitting. It is also seen from Figure 3 that the strongest absorption lines from $J = 1$ and 3 levels are slightly saturated and therefore their equivalent widths are sensitive to the assumed broadening model. The data for these levels give the effective Doppler width $b \simeq 3$ km s$^{-1}$. We also depicted two curves for $b = 2$ and 4 km s$^{-1}$ to demonstrate the complete consistency of $b$-values estimated in both approaches.

We note that Jenkins & Peimbert (1997) have measured an interesting phenomenon of increasing $b$-values for $H_2$ lines arising from progressively higher rotational levels in a spectrum of $\zeta$ Ori A. The most probable Doppler parameters were found to be $b(0) = 0.8$ km s$^{-1}$, $b(1) = 2.7$ km s$^{-1}$, $b(2) = 5.3$ km s$^{-1}$, $b(3) = 5.9$ km s$^{-1}$, and $b(5) = 9.0$ km s$^{-1}$. As they noted, such profile shapes are inconsistent with a simple model of UV optical pumping which governs the $H_2$ rotational populations in an optically thin, homogeneous medium. They suggested that these $H_2$ profiles with changing shapes "may represent molecules forming in the post-shock gas that is undergoing further compression as it recombines and cools." A similar phenomenon may also be observed in high-redshift DLA systems which can be associated to star-forming regions where shocks are very probable.

The $z_{abs} = 3.025$ system presents the weakest members of the Lyman and Werner series with $J = 4$ and 5, but, unfortunately, we are unable to compare their $b$-values with those from lower rotational transitions because our S/N is not sufficiently high. Thus, in the following we assume a simple one-component model for the molecular cloud with a common broadening parameter $b_{H_2} = 2.80$ km s$^{-1}$ for all molecular hydrogen lines.

[8] In the present paper, the estimated standard errors are slightly larger than those calculated by the Monte Carlo method because the pipeline resampling to constant wavelength bins introduces a correlation between data point values, whereas the estimated mean values of the physical parameters remain unbiased (see Appendix A).

### 3.3. $H_2$ *Abundances*

In the final fitting of each line profile we combined together the $H_2$ lines with the same $J$ to yield the corresponding $N(J)$ column densities and their confidence regions. A $\chi^2$ minimization procedure was applied simultaneously to all lines from a given rotational level $J$. To control solutions at this stage, we added to the lines listed in Table 1 a few weaker transitions where we observe continuum without any pronounced absorption features at their expected positions. The calculated $\chi^2_{\rm min}$ values and the 1 and 2 $\sigma$ confidence levels for each individual rotational level $J$ are shown in Figure 4. The curves $\chi^2[N(J)]$ were computed with the fixed mean $b_{H_2} = 2.80$ km s$^{-1}$ and the mean $z_{H_2}$. The $H_2$ lines involved in the analysis are as follows: L3-0R0 and L7-0R0 ($\mathcal{N} = 22$); L3-0P1 and L14-0P1 ($\mathcal{N} = 20$); W0-0R2, W0-0Q2, L3-0R2, L4-0R2, and L5-0R2 ($\mathcal{N} = 51$); W2-0R3, L2-0R3, L2-0P3, L3-0R3, L3-0P3, L4-0R3, L6-0R3, L7-0P3, L8-0P3, L12-0R3, and L15-0R3 ($\mathcal{N} = 83$); L5-0R4, L6-0R4, and L8-0P4 ($\mathcal{N} = 34$); L7-0P5 and L12-0R5 ($\mathcal{N} = 21$). The most probable column densities and their errors at the 1 $\sigma$ confidence level are $N(0) = (1.90 \pm 0.35) \times 10^{13}$ cm$^{-2}$, $N(1) = (1.60 \pm 0.18) \times 10^{14}$ cm$^{-2}$, $N(2) = (5.40 \pm 0.35) \times 10^{13}$ cm$^{-2}$, $N(3) = (1.22 \pm 0.05) \times 10^{14}$ cm$^{-2}$, $N(4) = (2.60 \pm 0.43) \times 10^{13}$ cm$^{-2}$, and $N(5) = (2.90 \pm 0.70) \times 10^{13}$ cm$^{-2}$. From that we calculate the total column density in $H_2$, $N(H_2) = \sum_J N(J) = (4.10 \pm 0.21) \times 10^{14}$ cm$^{-2}$, and the ratio of the total column densities in the ortho- and para-$H_2$ states $N_{\rm ortho}/N_{\rm para} = 3.1 \pm 0.3$ (s.d.). This result can be compared with two other molecular clouds at $z_{\rm abs} = 2.8112$ (Q0528$-$250; Srianand & Petitjean 1998) and $z_{\rm abs} = 2.33771$ (Q1232+0815; Srianand, Petitjean, & Ledoux 2000) where $N(J)$ values were also measured for different $J$. Using the published $N(J)$ values and their errors, we found $N_{\rm ortho}/N_{\rm para} = 3.1 \pm 0.8$ (s.d.) at $z_{\rm abs} = 2.8112$ and $N_{\rm ortho}/N_{\rm para} = 2.4 \pm 0.9$ (s.d.) at $z_{\rm abs} = 2.33771$.

According to our calculations presented in § 3.6, the total H I column density in the $z_{\rm abs} = 3.025$ system is $(4.225 \pm 0.045) \times 10^{20}$ cm$^{-2}$. With $N(H_2) = (4.10 \pm 0.21) \times 10^{14}$ cm$^{-2}$, the ratio of H nuclei in molecules to the total H nuclei is

$$f_{H_2} = \frac{2N(H_2)}{N(H)} = (1.94 \pm 0.10) \times 10^{-6} .$$

To test the consistency of the estimated physical parameters with the observed absorption features, we calculated theoretical profiles for all 88 $H_2$ lines using the derived mean $z_{H_2}$, $b_{H_2}$, and $N(J)$ values. Besides, we calculated eight profiles for $H_2$ transitions where no absorption features have been observed at the continuum level. The latter are L3-0R4, L9-0R4, L4-0R5, L9-0R5, L11-0P5, W0-0Q5, L6-0P6, and L7-0R7. The last two of them give upper limits to $N(6) < 2.0 \times 10^{13}$ cm$^{-2}$ (1 $\sigma$ c.l.) and $N(7) < 8.0 \times 10^{12}$ cm$^{-2}$ (1 $\sigma$ c.l.).

The observational and overplotted theoretical $H_2$ profiles are shown in Figures 5 and 6. In these figures possible blends with other lines from the $z_{\rm abs} = 3.025$ DLA and from the metal systems listed in Appendix B are also indicated. We found only one large inconsistency between observable and theoretical profiles, namely, for the W2-0Q(3) line (Fig. 6). However, in this case a very wide absorption trough between 3901 and 3921 Å redward of the redshifted position of this molecular line ($\lambda_{\rm obs} = 3900.3$ Å) prevents the accurate estimation of the local continuum level. Uncertainties in the local continuum level calculations may also cause overabsorption in the synthetic profiles as compared with the observable profiles seen in W1-0R0+R1, W2-0Q1 (Fig. 5), W0-0Q3, L3-0P3, L4-0P3, L10-0R3, L12-0R3, W0-0Q5, and L4-0R5 (Fig. 6). In all other cases the synthetic $H_2$ profiles are in agreement with the absorption-line features identified with the $H_2$ lines in the UV spectrum of Q0347$-$3819.

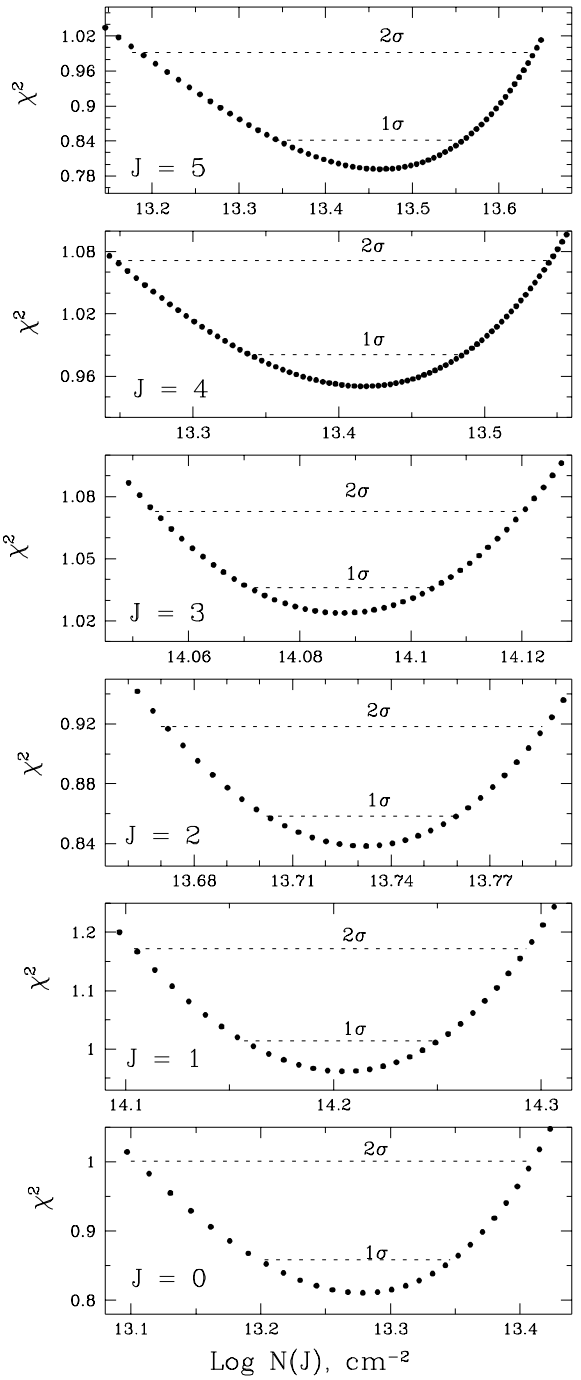


FIG. 4.—Confidence regions in the "$\chi^2$– log $N(J)$" planes calculated from the simultaneous fits of the $H_2$ lines arising from the same $J$ levels. The parabola vertexes correspond to the most probable values of $N(0) = 1.90 \times 10^{13}$ cm$^{-2}$, $N(1) = 1.60 \times 10^{14}$ cm$^{-2}$, $N(2) = 5.40 \times 10^{13}$ cm$^{-2}$, $N(3) = 1.22 \times 10^{14}$ cm$^{-2}$, $N(4) = 2.60 \times 10^{13}$ cm$^{-2}$, and $N(5) = 2.90 \times 10^{13}$ cm$^{-2}$.

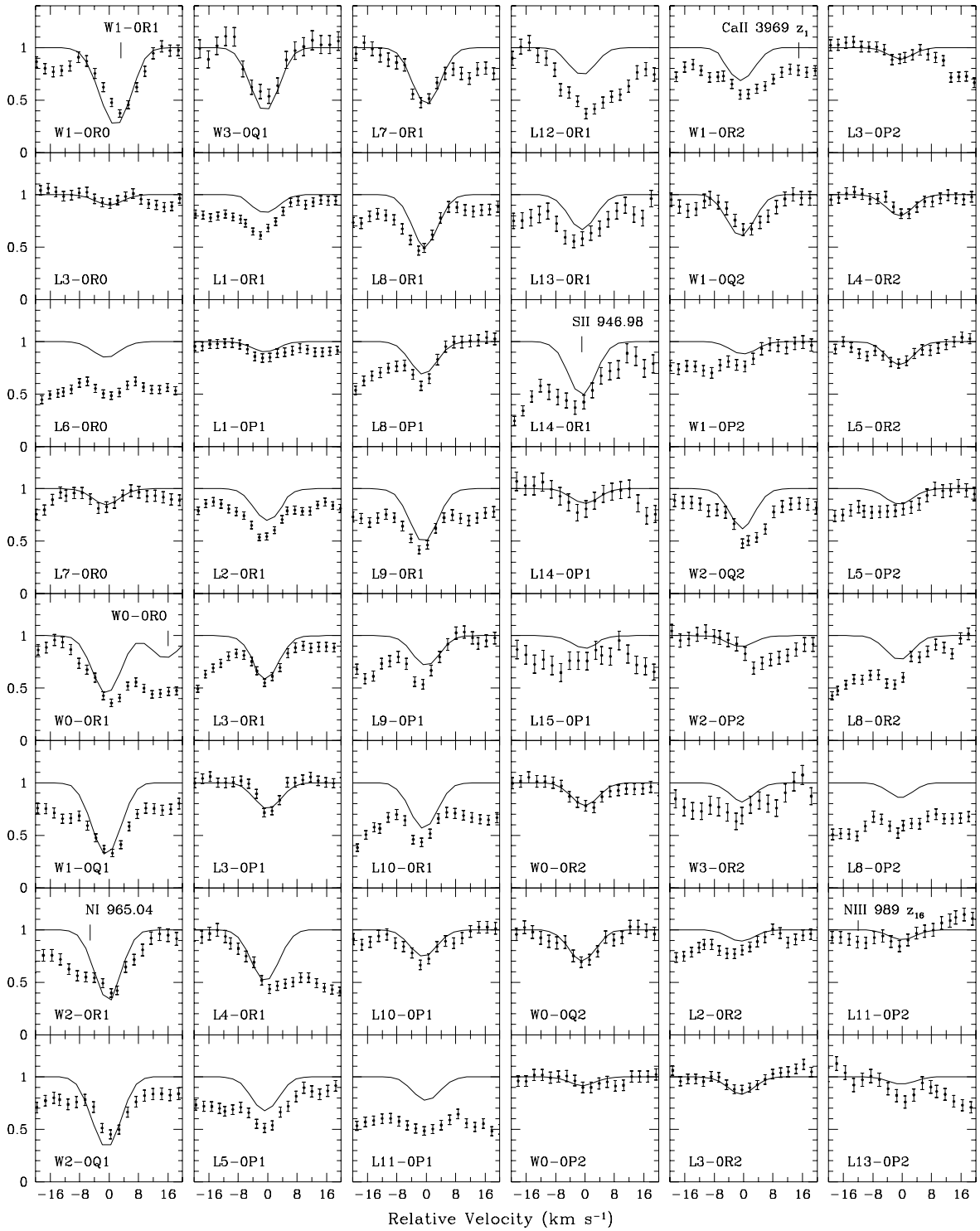


FIG. 5.—$H_2$ absorption features associated with the $z_{abs} = 3.025$ DLA system toward Q0347−3819 (normalized intensities are shown by filled circles with 1 $\sigma$ error bars). The zero radial velocity is fixed at $z_{H_2} = 3.024855$. Smooth lines are the synthetic $H_2$ spectra calculated for the mean physical parameters (see text). Possible blends with lines from the $z_{abs} = 3.025$ system are shown without indicating redshift, whereas blends with lines from other systems are indicated by ionic species with redshifts in accord with the list in Appendix B. $H_2$ profiles disturbed by the Ly$\alpha$ forest absorption are also included.

We have also tried to detect the $H_2$ molecules in the blue component at $\Delta v \simeq -17$ km s$^{-1}$ (see § 3.6) with respect to the main $H_2$-bearing component, but we found only an upper limit. The applied method is similar to that employed by Levshakov et al. (1989) to improve the detectability of weak carbon monoxide (CO) UV lines in DLA systems.

The procedure consists of shifting the observed spectral regions containing expected positions of the $H_2$ transitions, which are not contaminated by the apparent Ly$\alpha$ forest absorption, into the relative velocity scale centered at $z = 3.024637$, the redshift of the blue subcomponent of the dominant metal absorption in the $z_{abs} = 3.025$ DLA, and of

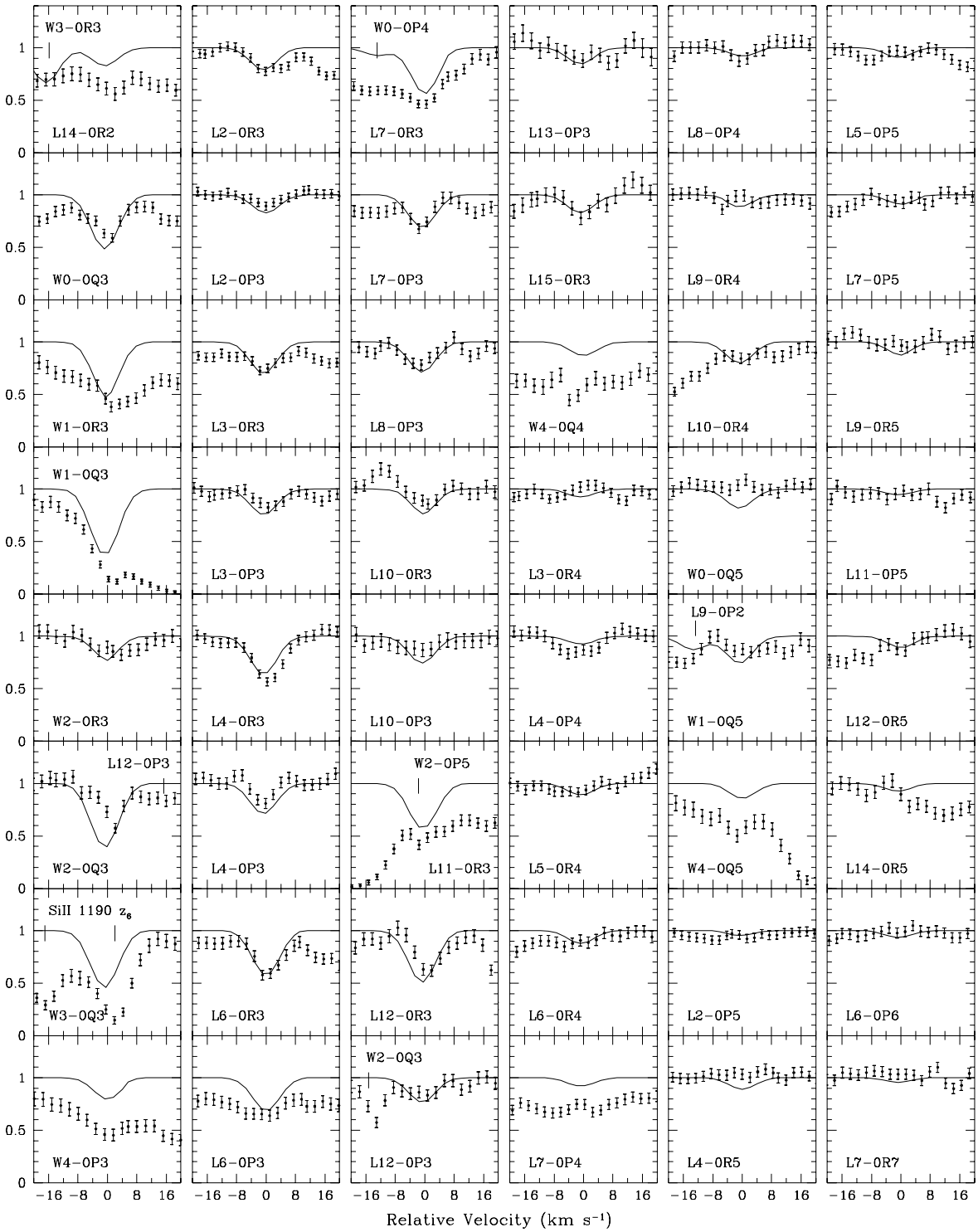


FIG. 6.—Same as Fig. 5

the consequent stacking of these regions. Before co-adding each section, the data are rebinned with a bin size of 1.45 km $s^{-1}$. The spectra were then averaged with weights in accord with the squares of the expected relative line strengths divided by the respective S/N values.

The result obtained from this stacking procedure is shown in Figure 7. The composite spectrum formed by the addition of 18 $H_2$ bands (with no pronounced absorption features in the range $\Delta v = \pm 6$ km $s^{-1}$), which are labeled in the corresponding panels, is depicted in the bottom panel. The resulting co-added data have an average S/N $\simeq$ 100 and show no absorption at $v = 0$ km $s^{-1}$, whereas the blue wing of the composed molecular line from the $z = 3.024855$ system is clearly seen at $v \simeq 16$ km $s^{-1}$.

The composite spectrum gives $W_{\lambda,\mathrm{rest}} < 0.6$ mÅ (3 $\sigma$ c.l.) for the equivalent width of the sum of the $H_2$ bands in the rest frame of the absorber. This limit is sensitive, in general, to errors in continuum fitting. In our case the resulting

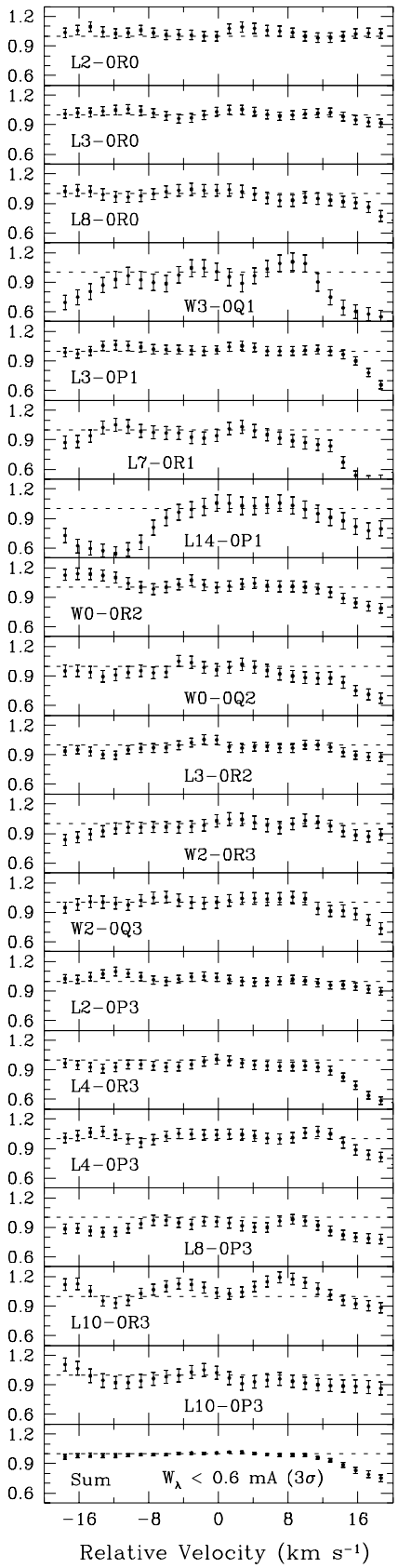


FIG. 7.—Spectral regions including the $H_2$ transitions of the Lyman and Werner bands (labeled in panels) in the $z = 3.024637$ absorber in the direction of Q0347−3819. The lowest panel presents the result of a stacking. The 3 $\sigma$ upper limit of 0.6 mÅ was calculated for a 12 km s$^{-1}$ window centered at $v = 0$ km s$^{-1}$.

profile between $-6 < v < 6$ km s$^{-1}$ has no apparent deviations from unity, the estimated mean value is $\langle C \rangle = 1.003 \pm 0.003$, and thus $\langle \sigma_c/C \rangle = 0.003$. Substituting these values in equation (3), we obtain the limiting equivalent width ($W' \ll 1$) $\sigma_{\rm lim} = 0.2$ mÅ and $W_{\lambda,\rm rest} = 0.6$ mÅ ($3\sigma_{\rm lim}$).

For a weak absorption line with the central optical depth $\tau_0 \ll 1$, the column density is independent of the broadening parameter $b$ and is linearly proportional to the equivalent width $W_\lambda$:

$$N = 1.13 \times 10^{20} \frac{W_\lambda}{\lambda_0^2 f} \text{ cm}^{-2} , \quad (5)$$

where $f$ is the oscillator strength for the absorption transition, $\lambda_0$ is the line-center rest wavelength in Å, and $W_\lambda$ is the rest equivalent width in Å.

Using this linear approximation to the curve of growth, we calculate the composite equivalent width $W_J$ for the $H_2$ bands from the same $J$ level:

$$W_J = aN_J \sum_i \lambda_{J,i}^2 f_{J,i} , \quad (6)$$

where $a = 8.85 \times 10^{-21}$. Then the total equivalent width for all $H_2$ bands presented in Figure 7 is

$$W_\Sigma = \sum_J W_J = a \sum_J \epsilon_J N_J = a\hat{\epsilon} N_{\rm H_2} , \quad (7)$$

where $\epsilon_J = \sum_i \lambda_{J,i}^2 f_{J,i}$, $\hat{\epsilon}$ is an effective value [in our estimation $\hat{\epsilon} = \max(\epsilon_J)$], and $N_{\rm H_2} = \sum_J N_J$.

The coefficients $\epsilon_J$ do not vary significantly, and for the $H_2$ bands from Figure 7 $\epsilon_0 = 6.1 \times 10^4$, $\epsilon_1 = 5.5 \times 10^4$, $\epsilon_2 = 5.3 \times 10^4$, and $\epsilon_3 = 9.8 \times 10^4$. Thus, the aforementioned upper limit $W_\lambda < 0.6$ mÅ and equation (7) yield $N(\rm H_2) < 7.0 \times 10^{11}$ cm$^{-2}$ (3 $\sigma$ c.l.) and $f_{\rm H_2} < 3.3 \times 10^{-9}$ (3 $\sigma$ c.l.), which is well below that found in Galactic H I clouds. It means that molecular hydrogen is not homogeneously distributed in the $z_{\rm abs} = 3.025$ absorbing region.

The measured $N_{\rm ortho}/N_{\rm para}$ ratios in the DLA systems at $z_{\rm abs} = 3.025$ (Q0347−3819), 2.8112 (Q0528−250), and 2.33771 (Q1232+0815) are equal to 3 (within the uncertainty interval), which is just the equilibrium value for the ortho:para ratio at the hot formation of $H_2$ on grain surfaces in relatively transparent clouds (e.g., Spitzer & Morton 1976). In the pristine gas, the ortho-$H_2$:para-$H_2$ ratio decreases from the equilibrium value of 3 at $z \simeq 100$ to its "freezeout" quantity of 0.25 at $z < 20$ (Flower & Pineau des Forêts 2000). Thus, we can conclude that $H_2$ observed in these DLA systems has undergone a reforming phase following photodissociation of the pristine $H_2$.

### 3.4. *Excitation Temperature*

In the ground electronic vibrational state, all the rotational levels with odd $J$ are nuclear triplet states (ortho-$H_2$) and all those with even $J$ are singlet states (para-$H_2$). Thus, for the ortho-$H_2$ the statistical weight, $g(J)$, of a level $J$ equals $3(2J + 1)$, whereas for the paramolecules $g(J) = (2J + 1)$. In thermal equilibrium, the collisionally dominated distribution of molecules over different $J$ levels is given by a Boltzmann law with an effective excitation temperature $T_{\rm ex}$:

$$\frac{N(J)}{N(0)} = \frac{g(J)}{g(0)} \exp\left[ -\frac{B_v J(J+1)}{T_{\rm ex}} \right] , \quad (8)$$

where the constant $B_v$ equals 85.36 K for the vibrational ground state.

This equation shows that $T_{ex}$ is proportional to the negative inverse of the slope of a line (called "the excitation diagram") drawn through the points of the respective $J$ levels in a plot log $[N(J)/g(J)]$ versus $E(J)$, where $N(J)$ is the column density measured in the rotational level $J$, $E(J)$ is the excitation energy of this level relative to $J = 0$, and $g(J)$ is its statistical weight. Figure 8 shows this diagram for different $J$ levels. A least-squares fit, weighted by $1/\sigma^2$ for each log $[N(J)/g(J)]$, yields $T_{ex} = 825 \pm 110$ K (s.d.) and log $[N(0)] = 13.31 \pm 0.03$ cm$^{-2}$ (s.d.). This value of $N(0)$ agrees well with what has been measured from profile fitting in § 3.3. Thus, we find that the population of the six lowest $J$ levels can be fitted with a single Boltzmann distribution.

The unique $T_{ex}$ for all levels from $J = 0$ to 5 may imply that the $H_2$ rotational population is dominated by collisions in a gas whose kinetic temperature is about 800 K. The kinetic temperature in the $H_2$ cloud can be estimated from the widths of the $H_2$ and metal lines. In § 3.6 we show that profiles of all metals from C II to Zn II can be described with the same broadening parameter of $b_{Me} = 2.71 \pm 0.05$ km s$^{-1}$. With $b_{H_2} = 2.80 \pm 0.45$ km s$^{-1}$, it gives an upper limit of $T_{kin} \leq 430$ K in the main $H_2$-bearing component. The fact that $T_{kin}$ is less than $T_{ex}$ indicates that the population of the low $J$ levels is caused not only by collisions but by UV pumping as well. The $J = 0$ and 1 rotational levels, being usually populated in dense molecular clouds by thermal proton collisions, may not be in equilibrium with the kinetic temperature in lower density clouds which are not optically thick in the L0-0R(0), R(1), P(1) and W0-0R(0), R(1), Q(1) lines. In low-density clouds the self-shielding effects are negligible and do not reduce significantly UV pumping in these lines (e.g., Shull & Beckwith 1982). For further analysis we set $T_{kin} = 400$ K to be consistent with the measured $b$-values.

### 3.5. Cr/Zn *and Dust Content*

The *Copernicus* $H_2$ survey has shown that in our Galaxy the molecular fraction $f_{H_2}$ is correlated with $E(B-V)$ and with the total neutral hydrogen column density (e.g., Spitzer & Jenkins 1975). The presence of dust grains in DLA systems is usually estimated from the abundance ratio [Cr/Zn][9] assuming that Zn is undepleted (Pettini et al. 1994).

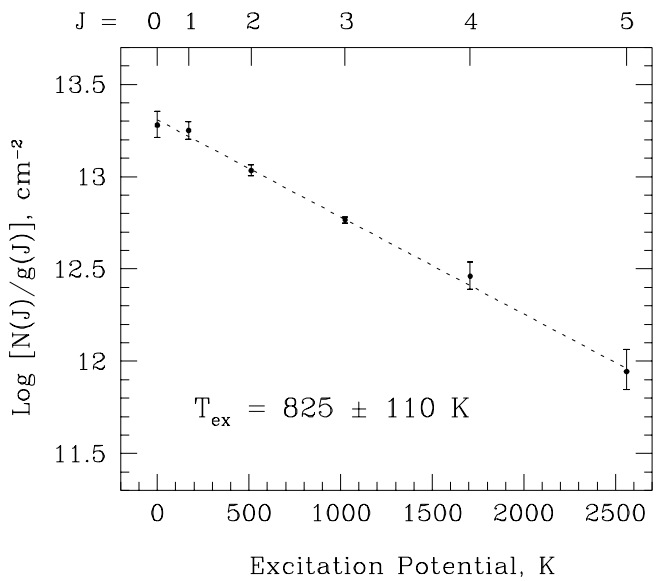


FIG. 8.—Population of the low rotational levels of $H_2$ in the $z_{abs} = 3.025$ DLA system toward Q0347−3819. Error bars for 1 $\sigma$ deviations are shown. The negative inverse slope of the best-fit straight dotted line indicates the excitation temperature of about 800 K.

Preliminary visual inspection of the red part of the Q0347−3819 spectrum has shown weak absorption features at the expected positions of Zn II and Cr II lines. In order to increase sensitivity and to measure the abundance ratio [Cr/Zn], we applied a stacking procedure similar to the one described in § 3.3 to the Zn II $\lambda\lambda$2026.136 and 2062.664 lines and to the Cr II $\lambda\lambda$2056.254, 2062.234, and 2066.161 lines. The wavelengths and the oscillator strengths for these lines are taken from Morton (1991) and Bergeson & Lawler (1993), respectively. The resulting composite spectra of Zn II and Cr II were included in the metal analysis in § 3.6. In the figure presented in the next section, two pronounced absorption features at $\Delta v \simeq 6$ km s$^{-1}$ (Cr II) and at $\Delta v \simeq 13$ km s$^{-1}$ (Zn II) are telluric lines. The former partly blends the red wing of the Cr II line, therefore we do not use this portion of the Cr II profile in the fitting procedure. The estimated total column densities are $N$(Zn II) = $(6.19 \pm 0.51) \times 10^{11}$ cm$^{-2}$ and $N$(Cr II) = $(2.76 \pm 0.22) \times 10^{12}$ cm$^{-2}$. With these numbers one finds [Cr/Zn] = $-0.37 \pm 0.06$.

In Table 2 we summarize the results of the abundance measurements of molecular hydrogen, [Cr/Zn] (and/or [Fe/Zn]), and neutral hydrogen in the DLA systems available up to now. The presence of dust in these DLA systems and the relation between the fractional molecular abundances and relative heavy-element depletion are illustrated in Figure 9. The measured data for the five extragalactic molecular clouds (marked by numbers in Fig. 9) can be fitted with a linear law: $\log f_{H_2} = A[\mathrm{Cr/Zn}] + B$, with $A = -6.053 \pm 0.116$ and $B = -7.888 \pm 0.051$. The linear regression is shown in Figure 9 by the solid line.[10] Again, similarly to our previously obtained results (Levshakov et al. 2000b), we find a strong correlation between $\log f_{H_2}$ in the DLA systems with detectable $H_2$ absorption and the heavy-element depletion. The presence of upper limits below the linear regression line may be explained by the suggestion that in these systems a relatively high temperature of dust grains prevents molecular formation.

The degree of the heavy-element depletion may be used to estimate the dust-to-gas ratio, $\tilde{k}$, if two measured elements have the same nucleosynthesis history (see Vladilo 1998):

$$\tilde{k} = \frac{10^{[\mathrm{Zn/H}]_{obs}}}{f_{Zn,ISM} - f_{Cr,ISM}} (10^{[\mathrm{Cr/Zn}]_{obs}} - 1) , \quad (9)$$

where the fraction in dust $f_{Zn,ISM} = 0.35$ and $f_{Cr,ISM} = 0.92$ refers to the Galactic interstellar medium.

Error propagation method applied to the column density measurements yields [Zn/H] = $-1.503 \pm 0.054$, and then

[9] $[X/Y] = (X/Y) - (X/Y)_\odot$, where $(X/Y)$ is the logarithmic value of the element ratio by number without reference to the solar value. Solar abundances $(X/Y)_\odot$ are taken from Grevesse & Sauval (1998).

[10] For the published 27 DLA systems where all three elements Zn II, Cr II, and Fe II were measured, [Cr/Fe] = $0.12 \pm 0.13$ (s.d.). This implies that Fe is slightly more depleted than Cr assuming that both elements track each other in the abundances and, thus, the slope in our regression analysis may be slightly steeper. However, the accuracy of the [Cr/Zn] and [Fe/Zn] measurements is not sufficiently high to provide an unambiguous renormalization of one element to the other. Therefore, [Fe/Zn] and [Cr/Zn] are used interchangeably in the present calculations.

TABLE 2

MOLECULAR HYDROGEN AND METAL ABUNDANCE MEASUREMENTS IN DLA SYSTEMS

| Number | QSO | $z_{abs}$ | [Cr/Zn] | [Fe/Zn] | log [$N$(H I)] | log [$N(H_2)$] | log $f_{H_2}$ |
|---|---|---|---|---|---|---|---|
| 1 ..... | Q1328+307 | 0.692 | $-0.44 \pm 0.10$[a] | ... | $21.28 \pm 0.10$[a] | $<15.70$[b] | $<-5.28$ |
| 2 ..... | Q0454+039 | 0.860 | $0.14 \pm 0.12$[c] | $0.01 \pm 0.12$[c] | $20.69 \pm 0.06$[c] | $<16.38$[b] | $<-4.01$ |
| 3 ..... | Q0935+417 | 1.373 | $-0.10 \pm 0.16$[d] | $-0.27 \pm 0.15$[d] | $20.40 \pm 0.09$[d] | $<16.40$[b] | $<-3.70$ |
| 4 ..... | Q1157+014 | 1.944 | ... | $-0.42 \pm 0.11$[e] | $21.80 \pm 0.10$[f] | $<14.71$[e] | $<-6.79$ |
| 5 ..... | Q0013−004 | 1.973 | $<-0.95$[g] | $-1.10 \pm 0.13$[g,h] | $20.70 \pm 0.05$[i] | $19.84 \pm 0.10$[i] | $-0.66 \pm 0.10$ |
| 6 ..... | Q0458−020 | 2.040 | $-0.36 \pm 0.05$[j] | $-0.46 \pm 0.07$[j] | $21.65 \pm 0.09$[g] | $<15.90$[b] | $<-5.45$ |
| 7 ..... | Q0100+130 | 2.309 | $-0.12 \pm 0.05$[j] | $-0.22 \pm 0.06$[j] | $21.40 \pm 0.05$[k] | $<15.70$[b] | $<-5.40$ |
| 8 ..... | Q1232+082 | 2.338 | ... | $-0.86 \pm 0.13$[l,m] | $20.90 \pm 0.10$[m] | $17.18 \pm 0.10$[m] | $-3.42 \pm 0.14$ |
| 9 ..... | Q0841+129 | 2.374 | $-0.12 \pm 0.08$[e,j] | $-0.29 \pm 0.08$[e] | $20.95 \pm 0.09$[j] | $<14.67$[e] | $<-5.98$ |
| 10 ..... | Q0112+029 | 2.423 | $-0.75 \pm 0.18$[g] | ... | $20.95 \pm 0.10$[g] | $<16.00$[b] | $<-4.65$ |
| 11 ..... | Q1223+178 | 2.466 | $-0.27 \pm 0.14$[g,e] | $-0.21 \pm 0.11$[e] | $21.52 \pm 0.10$[e] | $<14.30$[e] | $<-6.92$ |
| 12 ..... | Q0528−250 | 2.811 | $-0.46 \pm 0.14$[n] | $-0.46 \pm 0.12$[n,o] | $21.35 \pm 0.10$[p,q] | $16.77 \pm 0.09$[r,o] | $-4.28 \pm 0.13$ |
| 13 ..... | Q0347−382 | 3.025 | $-0.37 \pm 0.06$[s] | $-0.19 \pm 0.06$[s] | $20.626 \pm 0.005$[s] | $14.613 \pm 0.022$[s] | $-5.71 \pm 0.02$ |
| 14 ..... | Q0000−262 | 3.390 | $0.06 \pm 0.07$[t] | $0.03 \pm 0.07$[t] | $21.41 \pm 0.08$[j] | $13.94 \pm 0.06$[u,v] | $-7.17 \pm 0.13$ |

NOTE.—Column densities $N$(H I) and $N(H_2)$ are given in $cm^{-2}$.

[a] Meyer & York 1992.
[b] Ge & Bechtold 1999.
[c] Pettini et al. 2000.
[d] Meyer, Lanzetta, & Wolf 1995.
[e] Petitjean et al. 2000.
[f] Wolfe & Briggs 1981.
[g] Pettini et al. 1994.
[h] Centurion et al. 2000.
[i] Ge & Bechtold 1997.
[j] Prochaska & Wolfe 1999.
[k] Wolfe et al. 1994.
[l] Ge, Bechtold, & Kulkarni 2001.
[m] Srianand et al. 2000.
[n] Lu et al. 1996.
[o] Srianand & Petitjean 1998.
[p] Levshakov & Foltz 1988.
[q] Møller & Warren 1993.
[r] Levshakov & Varshalovich 1985.
[s] This paper.
[t] Molaro et al. 2000.
[u] Levshakov et al. 2000b.
[v] Levshakov et al. 2001.

equation (9) results in the average value for the whole DLA $\tilde{k}_{DLA} = 0.032 \pm 0.005$ (1 $\sigma$ c.l.) showing that the dust content in the $z_{abs} = 3.025$ absorber is approximately 30 times lower as compared with the Milky Way. If, however, we consider the same quantity for the $H_2$-bearing cloud using the data from Table 3, then $\tilde{k} \simeq 0.047$, i.e., the dust content in the molecular cloud is about 1.5 times higher as compared with the average value.

### 3.6. D/H *and Metal Abundances*

In this section we study metal profiles and derive a new D/H ratio by fitting simultaneously the available Lyman series lines and metals. The knowledge of the proper distribution of the velocity components along the line of sight is especially crucial for the D/H measurements, since D I lines are always blended with the blue wings of the corresponding H I lines (for numerous examples see Levshakov, Kegel, & Takahara 1999a and references therein).

In the UVES spectrum of Q0347−3819, at $z_{abs} = 3.025$ we have identified absorption lines of C II, N I, O I, Si II, P II, Ar I, Cr II, Fe II, Zn II, and C II*. The identified metal absorption lines are shown in Figure 10, and the atomic hydrogen lines are shown in Figure 11. The atomic data were taken mainly from Morton (1991) with a few additions of new results for Si II from Spitzer & Fitzpatrick (1993) and Charro & Martín (2000), for Ar I from Federman et al. (1992), for Cr II and Zn II from Bergeson & Lawler (1993), and for Fe II from Cardelli & Savage (1995), Raassen & Uylings (1998), and Howk et al. (2000).

To construct a model for the radial velocity distribution, we first analyzed the profiles of each individual atom/ion to select lines (or parts of them) which are less contaminated and disturbed by the Ly$\alpha$ forest absorption. The chosen profiles and/or their components are marked in Figures 10 and 11 by horizontal lines at the bottoms of the panels (these horizontal lines also show the pixels involved in the final optimization procedure). Other spectra in Figures 10 and 11, not marked by the horizontal lines, were used to control consistency of the obtained results.

Our model is based on the following assumptions: (1) the whole DLA is considered as a continuous absorbing region with fluctuating gas density and velocity fields; (2) the metallicity for each element is set constant through the DLA; and (3) some of the observed species may have similar profiles, i.e., their fractional ionization ratios remain constant along the sight line. In this case complex profiles can be modeled using the sum of the same number of components with identical centers and equal relative intensities for any pair of lines (Levshakov, Takahara, & Agafonova 1999b).

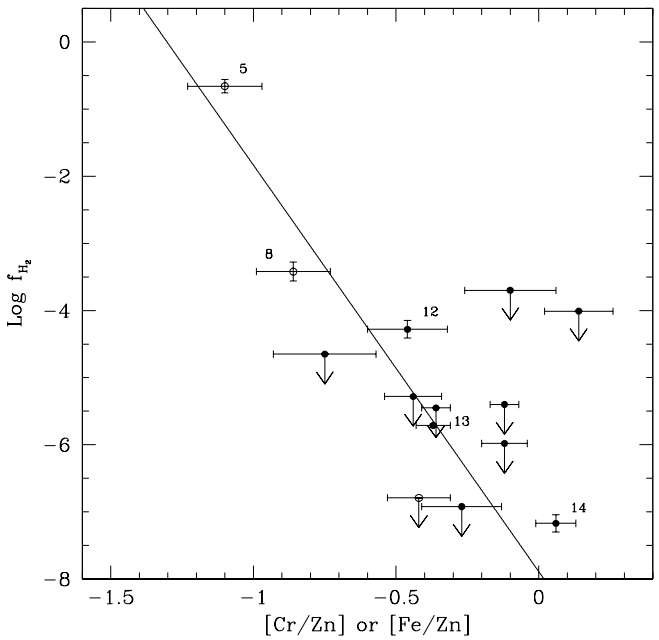


FIG. 9.—Relation between $H_2$ fractional abundance $f_{H_2}$ plotted on a logarithmic scale and relative heavy-element depletion in DLA systems. The solid line corresponds to the linear law: $\log f_{H_2} \simeq -6.1[\mathrm{Cr/Zn}] - 7.9$, obtained for the five measurements of $f_{H_2}$ we know (DLA systems 5, 8, 12, 13, and 14). The filled circles correspond to [Cr/Zn] and the open ones to [Fe/Zn]. See Table 2 for references.

The line profiles are described by the sum of $m$ Voigt functions:

$$\tau_\lambda = \sum_{i=1}^{m} N_i \, \mathscr{V}\left[\frac{\lambda - \lambda_0 - \lambda_0(v_i/c)}{\Delta\lambda_i}\right], \qquad (10)$$

where $\tau_\lambda$ is the optical depth at wavelength $\lambda$ within the line profile, $N_i$ is the column density in the $i$th component, $v_i$ is its Doppler shift, and $\Delta\lambda_i = \lambda_0 b_i/c$ is its Doppler width with $c$ being the speed of light and $\lambda_0$ the line center.

Equation (10) requires an additional suggestion about the broadening mechanism. We assume that the main broadening is caused by bulk motion. For the component seen in the $H_2$ lines this suggestion is supported by the measured equivalence of $b_{H_2}$ and $b_{Me}$, whereas for other components it is a model assumption which has to be checked during the optimization procedure.

Now we can describe our model in detail. It is fully defined by specifying $\{N_i\}_{i=1}^{\kappa}$, the column density of the first components for each ion, with $\kappa$ being the total number of ions; $\{\mathscr{R}_{1i}\}_{i=2}^{m}$, the relative intensities of the subcomponents, where for a given ion $\mathscr{R}_{1i} = N_i/N_1$; $\{v_i\}_{i=1}^{m}$, the Doppler shifts; and $\{b_i\}_{i=1}^{m}$, the Doppler widths. All these parameters are components of the parameter vector $\theta = \{\theta_1, \theta_2, \ldots, \theta_q\}$. In addition to $\theta$, the D/H ratio is to be set. To estimate $\theta$ from the absorption-line profiles, we minimize the objective function

$$\chi^2\left(\frac{\mathrm{D}}{\mathrm{H}}\right) = \frac{1}{\nu} \frac{\sum_{\ell=1}^{L} \sum_{i=1}^{M_\ell} [\mathscr{F}^{\mathrm{obs}}_{\ell,\lambda_i} - \mathscr{F}^{\mathrm{cal}}_{\ell,\lambda_i}(\theta)]^2}{\sigma^2_{\ell,i}}, \qquad (11)$$

where D/H is the total hydrogen isotopic ratio for the whole system. $\mathscr{F}^{\mathrm{obs}}_{\ell,\lambda_i}$ is the observed normalized intensity of the spectral line $\ell$, and $\sigma_{\ell,i}$ is the experimental error within the $i$th pixel of the line profile. $\mathscr{F}^{\mathrm{cal}}_{\ell,\lambda_i}(\theta)$ is the calculated intensity of line $\ell$ at the same $i$th pixel having wavelength $\lambda_i$:

$$\mathscr{F}^{\mathrm{cal}}_{\ell,\lambda_i}(\theta) = \int e^{-\tau_{\ell,\lambda_i}(\theta)} \phi_{\mathrm{PSF}}(\lambda_i - \lambda) d\lambda, \qquad (12)$$

where $\tau_{\ell,\lambda_i}(\theta)$ is defined through equation (10). The instrumental PSF $\phi_{\mathrm{PSF}}(\lambda)$ is approximated by a Gaussian with FWHM = 7.0 km s$^{-1}$ (see § 3.2).

The total number of spectral lines involved in the optimization procedure is labeled by $L$, and the total number of data points $\mathscr{M} = \sum_\ell^L M_\ell$, where $M_\ell$ is the number of data points for the $\ell$th line. The number of degrees of freedom is labeled by $\nu$.

After preliminary trial computations we were able to separate all available lines into two groups consisting of

TABLE 3

COLUMN DENSITIES AND RELATIVE ABUNDANCES IN THE $H_2$-BEARING CLOUD AT $z_{\mathrm{abs}} = 3.025$ TOWARD Q0347−3819

| Ion | log $N$ (cm$^{-2}$) | $(\mathrm{X/H})^{a}_{\odot}$ | [X/H] | [X/Zn] |
|---|---|---|---|---|
| H I..... | 20.402 ± 0.006[b] | ... | ... | ... |
| C I..... | <11.6[c,d] | ... | ... | ... |
| C II* ..... | 13.354 ± 0.023 | ... | ... | ... |
| C II ..... | 15.703 ± 0.024 | −3.48 ± 0.06 | −1.22 ± 0.06 | 0.29 ± 0.08 |
| N I..... | 14.664 ± 0.007 | −4.08 ± 0.06 | −1.66 ± 0.06 | −0.15 ± 0.08 |
| O I* ..... | <11.9[c,d] | ... | ... | ... |
| O I..... | 16.410 ± 0.010 | −3.17 ± 0.06 | −0.82 ± 0.06 | 0.69 ± 0.08 |
| Si II*..... | <12.4[c,d] | ... | ... | ... |
| Si II ..... | 15.015 ± 0.013 | −4.44 ± 0.05 | −0.95 ± 0.02 | 0.56 ± 0.06 |
| P II ..... | 12.779 ± 0.032 | −6.44 ± 0.06 | −1.18 ± 0.07 | 0.32 ± 0.09 |
| Ar I..... | 13.760 ± 0.020 | −5.48 ± 0.04[e] | −1.16 ± 0.05 | 0.35 ± 0.07 |
| Cr II ..... | 11.698 ± 0.046 | −6.31 ± 0.01 | −2.39 ± 0.05 | −0.89 ± 0.07 |
| Fe II ..... | 13.690 ± 0.032 | −4.50 ± 0.01 | −2.21 ± 0.03 | −0.71 ± 0.06 |
| Zn II ..... | 11.565 ± 0.037 | −7.33 ± 0.04 | −1.51 ± 0.05 | ... |

[a] Grevesse & Sauval 1998.
[b] Indicated are the internal errors.
[c] 1 $\sigma$ level.
[d] Based on the Keck/HIRES data obtained by Prochaska & Wolfe 1999.
[e] Sofia & Jenkins 1998.

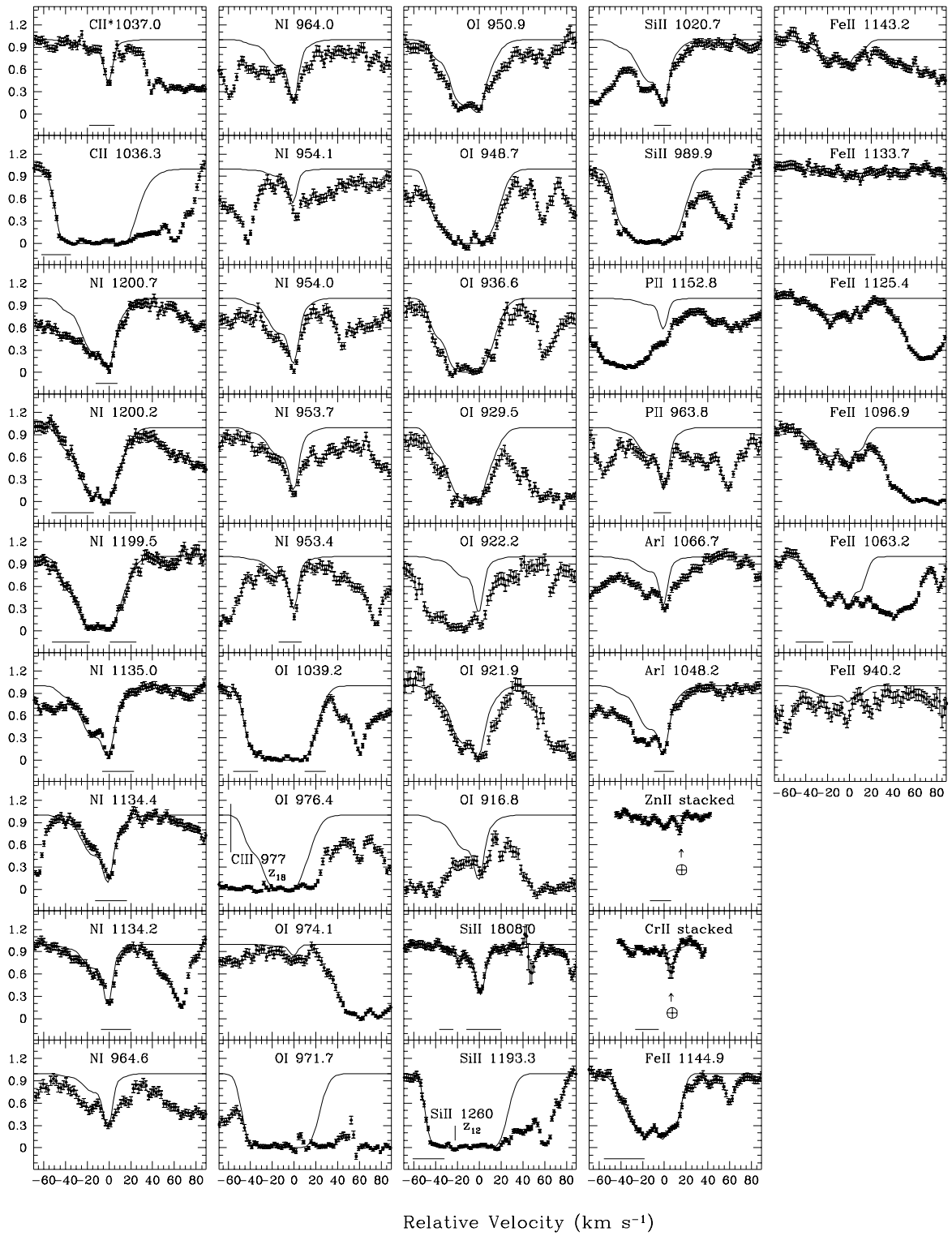


FIG. 10.—Metal absorption features associated with the $z_{abs} = 3.025$ DLA toward Q0347−3819 (normalized intensities are shown by filled circles with 1 $\sigma$ error bars). The zero radial velocity is fixed at $z_{abs} = 3.024855$. The smooth lines are the synthetic spectra convolved with the instrumental resolution of FWHM = 7.0 km s$^{-1}$. Two groups of lines (H I, C II, C II*, N I, O I, Si II, P II, Ar I, Zn II and Fe II, Cr II) are fitted simultaneously to the observed profiles or to their portions marked by horizontal lines which also indicate pixels involved in the optimization procedure (the corresponding hydrogen profiles are shown in Figs. 11 and 12). For Zn II and Cr II composite stacked spectra are shown. Two absorption features at $\Delta v \simeq 17$ km s$^{-1}$ (Zn II) and $\Delta v \simeq 6$ km s$^{-1}$ (Cr II) are telluric lines. Possible blends with lines from other systems are indicated by ionic species with redshifts in accord with the list in Appendix B.

similar profiles (the fitting of each group of lines yielded acceptable $\chi^2$ values). Similarity in this context means that the density-weighted radial velocity distribution functions for elements combined in a group are equal (see eq. [15] and explanations below). The first group includes $\kappa = 9$ different ions (H I, C II, C II*, N I, O I, Si II, P II, Ar I, and Zn II) with the total number of data points $\mathcal{M} = 566$ and $\nu = 544$ (we consider C II* as a separate element since it has

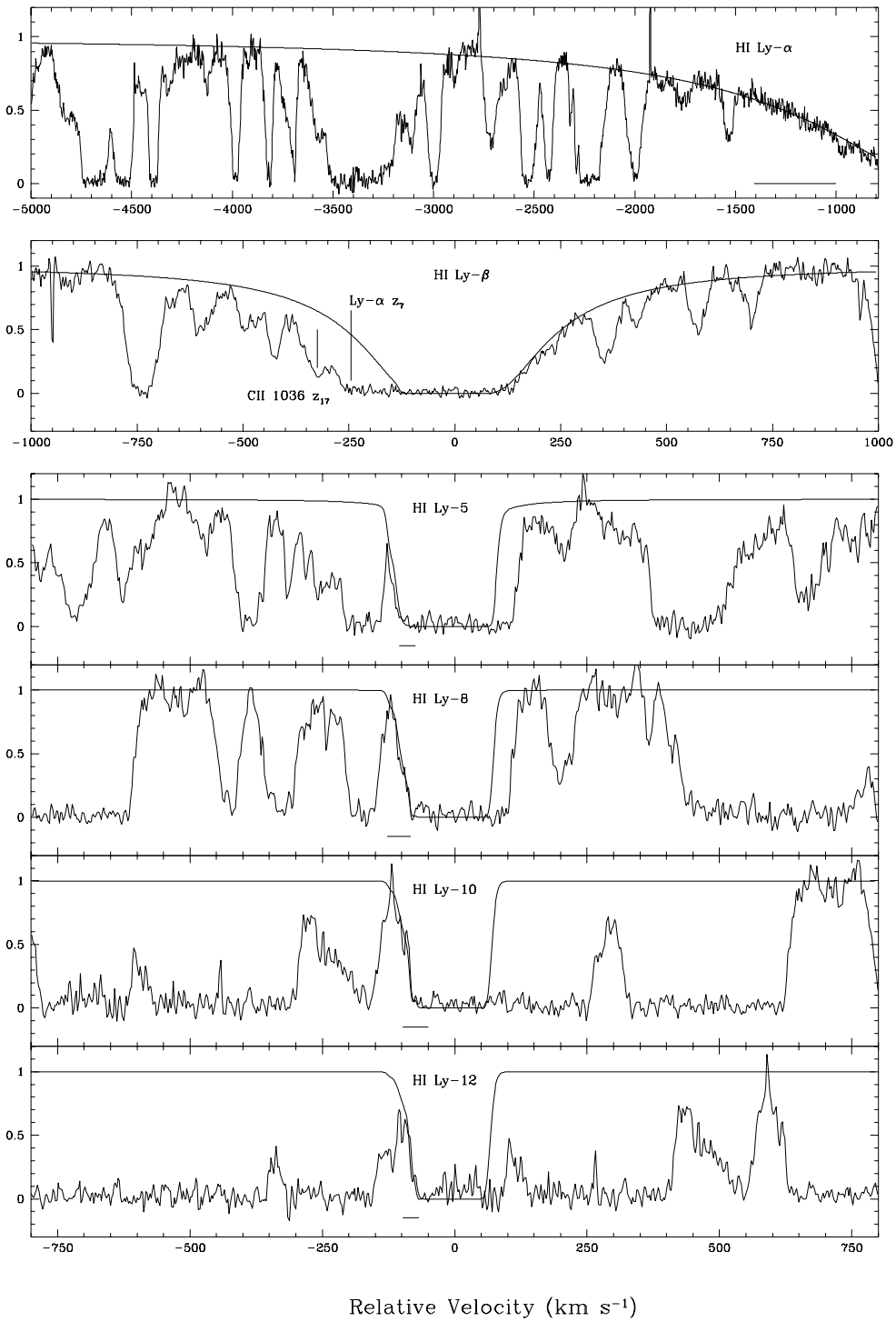


FIG. 11.—Same as Fig. 10, but for the hydrogen and deuterium lines. For the Ly$\alpha$ line only a portion of its blue wing free of the forest absorptions is shown. The blue wing of Ly$\beta$ is contaminated by the forest absorption. The deuterium absorption seen in Ly8, Ly10, and Ly12 is shown zoomed in Fig. 12. The corresponding D/H ratio is equal to $3.75 \times 10^{-5}$.

a column density different from C II). The second one consists of $\kappa = 2$ ions (Fe II and Cr II) with $\mathscr{M} = 110$, $v = 99$. These two groups are essentially the refractory and nonrefractory (or little refractory) elements.

We do not consider the absorption features seen at $\Delta v \simeq 40$ and 60 km s$^{-1}$ in the C II $\lambda$1036.3, N I $\lambda$1134.2, O I $\lambda$1039.2, and Si II $\lambda$1193.3 profiles (Fig. 10) since we are mostly interested in the main $H_2$-bearing component ($\Delta v = 0$ km s$^{-1}$) and the blue side parts of the profiles which restrict the configuration of the velocity field important for the analysis of the observed D I lines. For this reason only blue parts of the H I Ly$\alpha$, Ly5, Ly8, Ly10, and Ly12 lines were included in the analysis (see Figs. 11 and 12). The components at $\Delta v \simeq 40$ and 60 km s$^{-1}$ increase the total column densities measured in the range $-50 \leq v \leq 80$ km s$^{-1}$ at about 8% only.

The estimation of the parameter vector $\theta$ by means of the $\chi^2$ minimization is a typical *ill-posed* problem (Tikhonov &

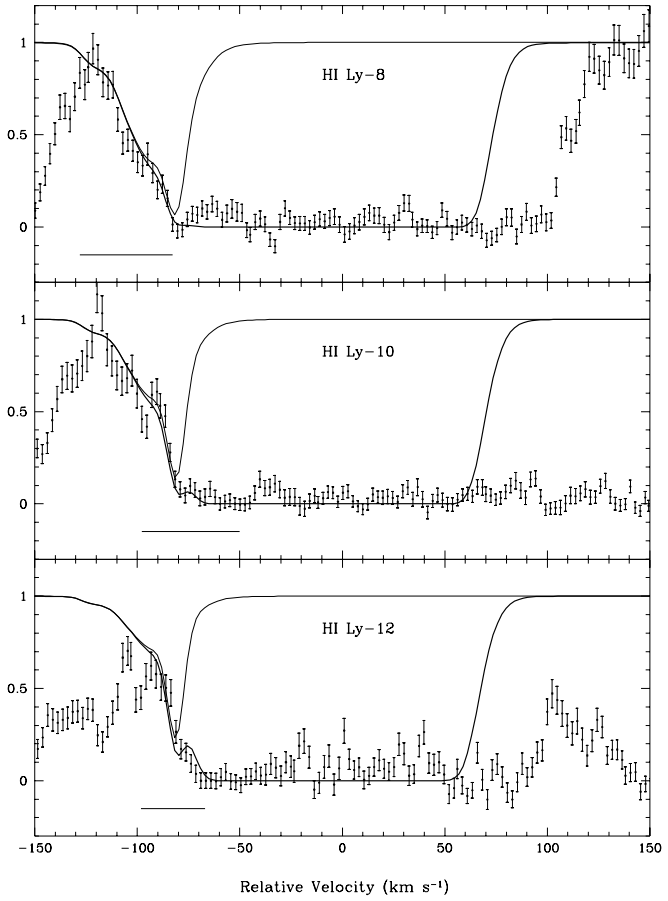


FIG. 12.—Same as Fig. 11 to show details of the H + D (*thick lines*) and D (*thin lines*) profiles.

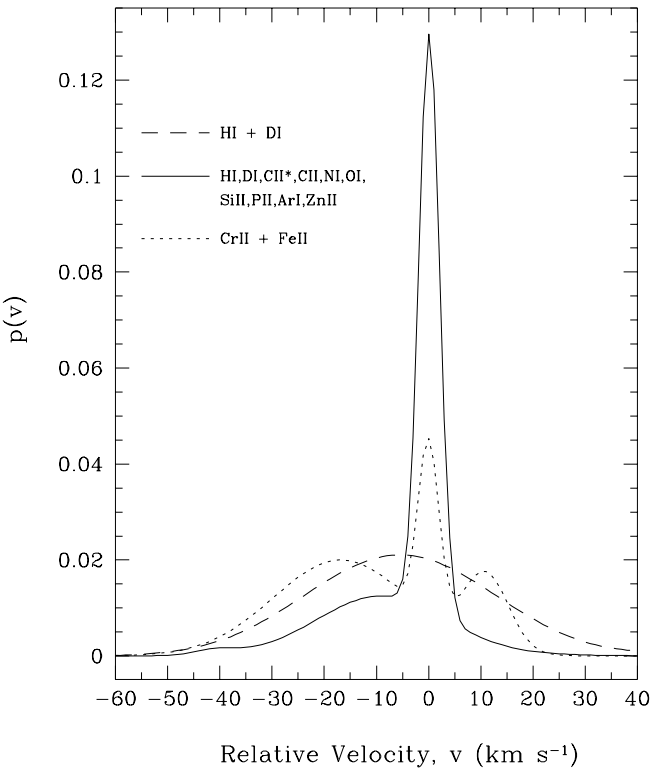


FIG. 13.—Radial velocity distributions $p(v)$ for the models adopted in the present paper (*solid and dotted curves*) and, for comparison, $p(v)$ from DDM01 (*dashed curve*). The difference in shapes of $p(v)$ leads to the difference in the estimations of D/H: $(2.24 \pm 0.67) \times 10^{-5}$ (DDM01) and $(3.75 \pm 0.25) \times 10^{-5}$ (see Fig. 14). The intense and narrow spike at $\Delta v \simeq 0$ km s$^{-1}$ was revealed from the analysis of the $H_2$ lines.

Arsenin 1977) because of the presence of two smoothing operators in equations (10) and (12) which prevent one from deducing a unique value of $\theta$. To stabilize the solution, we augment $\chi^2$ by a regularization term in a way similar to that discussed in Levshakov et al. (1999b): instead of minimizing $\chi^2$, defined in equation (11), we now seek the minimum of another objective function,

$$\mathscr{L}_\alpha(\theta) = \chi^2(\theta) + \alpha\psi(\theta) , \qquad (13)$$

where $\psi$ is a penalty function and $\alpha$ the regularization parameter.

The choice of $\psi$ for nonlinear problems occurs rather heuristically. For our particular DLA we used additional information obtained from the analysis of $H_2$. Namely, we searched for the minimum of $\mathscr{L}_\alpha(\theta)$ in the vicinity of the main component (i.e., $\Delta v_{H_2} \simeq 0$ km s$^{-1}$), which is supposed to have $b \simeq b_{H_2}$. Then the easiest choice for $\psi$ will be

$$\psi = \left(\frac{b - b_{H_2}}{\sigma_{b_{H_2}}}\right)^2 + (\Delta v - \Delta v_{H_2})^2 , \qquad (14)$$

and we set the regularization parameter $\alpha = 1$.

The importance of the regularization is illustrated in Figure 13, where different velocity distribution functions $p(v)$ are shown. The differences in shapes of $p(v)$ may cause different D/H values. For instance, being analyzed separately, the H + D profiles yield a shallow and smoother $p(v)$ (Fig. 13, *dashed curve*), whereas a simultaneous fitting with metals reveals a sharp spike at $\Delta v \simeq 0$ km s$^{-1}$ (*solid curve*) and a slightly different structure of the blue wing of $p(v)$ at $\Delta v < -5$ km s$^{-1}$. The difference in D/H is, indeed, essential: D/H $= (2.24 \pm 0.67) \times 10^{-5}$ in the former case (see DDM01) and D/H $= (3.75 \pm 0.25) \times 10^{-5}$ in the latter one (see Fig. 14).

The estimated column densities together with their errors and relative abundances in the $H_2$-bearing cloud are listed in Table 3. The errors were calculated by using the $\Delta\chi^2$ method. They reflect internal uncertainties of the physical parameters within the adopted model. Total column densities (calculated in the range $-50 \le v \le 20$ km s$^{-1}$) for all elements, their relative abundances, and corresponding errors are listed in Table 4. Besides, we also estimated in the main component 1 $\sigma$ upper limits to $N$(C I) $< 4.2 \times 10^{11}$ cm$^{-2}$ from the C I $\lambda$1277.2 line, to $N$(O I*) $< 8.2 \times 10^{11}$ cm$^{-2}$ from the O I* $\lambda$1304.8 line, and to $N$(Si II*) $< 2.6 \times 10^{12}$ cm$^{-2}$ from the Si II* $\lambda$1533.4 line using the Keck telescope spectrum of Q0347−3819 obtained by Prochaska & Wolfe (1999). These data are included in Table 3. The most probable $b$ parameters, corresponding to the column densities from Table 3, are $b_{\mathrm{H\,I+Me}} = 2.71 \pm 0.05$ km s$^{-1}$ and $b_{\mathrm{Cr\,II+Fe\,II}} = 2.80 \pm 0.26$ km s$^{-1}$. It shows that in spite of the difference in shapes of $p(v)$ for two groups of ions, the broadening parameter in the central $H_2$-bearing component is the same.

The measured value of log [$N$(H I)] $= 20.626 \pm 0.005$ cm$^{-2}$ is in good agreement with the DDM01 measurement of log [$N$(H I)] $= 20.63 \pm 0.09$ cm$^{-2}$. The recalculated

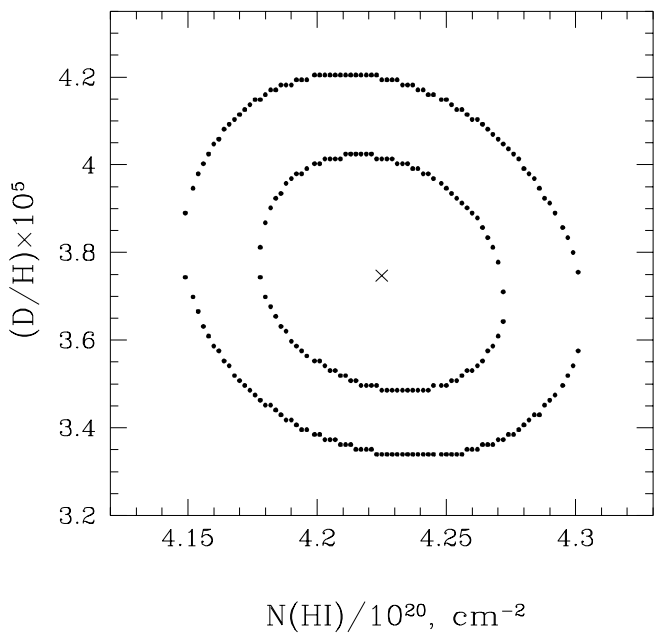


FIG. 14.—Confidence regions in the "H I–D/H" plane calculated from the simultaneous fit of the H I and metal lines shown in Figs. 10 and 11 when the other best-fitting parameters of the adopted model are fixed. The contours represent 68.3% (*inner*) and 95.4% (*outer*) confidence levels. The cross marks the point of maximum likelihood for the adopted model ($\chi^2_{\rm min} = 1.22, \nu = 545$).

value of D/H = $(3.75 \pm 0.25) \times 10^{-5}$ is consistent with standard big bang nucleosynthesis predictions (e.g., Burles et al. 1999) if the baryon-to-photon ratio, $\eta$, is in the range $4.37 \times 10^{-10} \lesssim \eta \lesssim 5.32 \times 10^{-10}$. With the present-day photon density determined from the cosmic microwave background radiation (CMBR; Mather et al. 1999), we can estimate the present-day baryon density $\Omega_b h^2_{100} \equiv 3.73 \times 10^7 (T_{\rm CMBR}/2.75)^3 \eta \simeq 0.016$–$0.020$.

Our new D/H ratio is shifted toward the higher hydrogen isotopic ratio found in the Lyman limit systems (LLSs) by Tytler et al. (2000), D/H = $(3.5 \pm 0.5) \times 10^{-5}$. We recall that the ratio of D/H $\simeq 4 \times 10^{-5}$ was found from the Tytler et al. (2000) LLSs using a different mesoturbulent method by Levshakov, Kegel, & Takahara (1998) and Levshakov, Tytler, & Burles (2000c). We thus summarize that when all most accurate measurements of D/H in high-redshift QSO absorbers are considered, one finds the same D/H value, which is about 2.5 times the mean ISM value of D/H = $(1.50 \pm 0.10) \times 10^{-5}$ (e.g., Linsky 1998).

To conclude this section, we comment on the fitting of the C II $\lambda$1036 line: the exact measurement of the column density for this ion is very important since the calculation of the volumetric gas density $n_{\rm H}$ in the $z_{\rm abs} = 3.025$ molecular cloud is based on the ratio of $N$(C II*)/$N$(C II). The C II $\lambda$1036 line is saturated, and having this line alone we would be able to estimate only a lower boundary for $N$(C II). However, the system under study exhibits plenty of other metal profiles which are unsaturated. Being fitted together with C II, these profiles allow us to restrict the shape of the radial velocity distribution $p(v)$ and then to determine the real column density of C II. As already stated above, the measurement of $N$(C II) from the saturated $\lambda$1036 line is possible if the density-weighted velocity distribution functions of C II and a match ion (which shows unsaturated absorption profiles) are equal.

Indeed, for a fixed value of $\lambda$ (or $v$ in the velocity space) within the line profile, the optical depth $\tau_{a,i}(\lambda)$ of element "$a$" in the $i$th ionization stage is given by (see eqs. [24]–[26] in Levshakov, Agafonova, & Kegel 2000a)

$$\tau_{a,i}(\lambda) = k_0 N_{a,i} \int_0^1 n_{\rm H}(x) \frac{\Upsilon_{a,i}[U(x)]}{\bar{\Upsilon}_{a,i}} \Phi_\lambda[\Delta\lambda_D(x), v(x)] dx \,, \tag{15}$$

where $k_0$ is a constant for a particular line, $N_{a,i}$ is the column density, $n_{\rm H}(x)$ is the volumetric gas density at point $x$, $\Upsilon_{a,i} = n_{a,i}/n_a$ is the fractional ionization, $U = n_{\rm ph}/n_{\rm H}$ is the ionization parameter with $n_{\rm ph}$ being the number of photons with energies above 1 ryd, $\Phi_\lambda$ is the profile function at the local velocity $v(x)$, and $\bar{\Upsilon}_{a,i}$ is the mean density-weighted fractional ionization.

TABLE 4

TOTAL COLUMN DENSITIES AND RELATIVE ABUNDANCES AT $z_{\rm abs} = 3.025$ TOWARD Q0347−3819[a]

| Ion | log $N$ ($\rm cm^{-2}$) | $(\rm X/H)_\odot$[b] | [X/H] | [X/Zn] | [X/H][c] | [X/H][d] | [X/H][e] |
|---|---|---|---|---|---|---|---|
| H I ..... | 20.626 ± 0.005[f] | ... | ... | ... | ... | ... | ... |
| C II ..... | 15.929 ± 0.024 | −3.48 ± 0.06 | −1.22 ± 0.06 | 0.29 ± 0.08 | ... | > −2.4 | > −2.2 |
| C II* ..... | 13.581 ± 0.024 | ... | ... | ... | ... | ... | ... |
| N I ..... | 14.890 ± 0.007 | −4.08 ± 0.06 | −1.66 ± 0.06 | −0.15 ± 0.08 | −2.1 | −2.5 | ... |
| O I ..... | 16.636 ± 0.011 | −3.17 ± 0.06 | −0.82 ± 0.06 | 0.68 ± 0.08 | > −1.5 | > −2.4 | > −2.2 |
| Si II..... | 15.240 ± 0.013 | −4.44 ± 0.05 | −0.95 ± 0.02 | 0.56 ± 0.06 | −1.2 | > −1.9 | −1.4 |
| P II ..... | 13.005 ± 0.031 | −6.44 ± 0.06 | −1.18 ± 0.07 | 0.32 ± 0.09 | ... | ... | ... |
| Ar I..... | 13.986 ± 0.020 | −5.48 ± 0.04[g] | −1.16 ± 0.04 | 0.34 ± 0.07 | ... | ... | ... |
| Cr II ..... | 12.441 ± 0.035 | −6.31 ± 0.01 | −1.88 ± 0.04 | −0.37 ± 0.06 | ... | ... | ... |
| Fe II ..... | 14.432 ± 0.009 | −4.50 ± 0.01 | −1.69 ± 0.01 | −0.19 ± 0.06 | −1.9 | > −2.0 | −1.7 |
| Zn II..... | 11.792 ± 0.036 | −7.33 ± 0.04 | −1.50 ± 0.05 | ... | < −0.8 | < −1.2 | ... |

[a] Listed values were measured in the range $-50 \le v \le 20$ km s$^{-1}$ (see Fig. 10).
[b] Grevesse & Sauval 1998.
[c] Centurión et al. 1998.
[d] Ledoux et al. 1998.
[e] Prochaska & Wolfe 1999.
[f] Indicated are the internal errors.
[g] Sofia & Jenkins 1998.

If the line broadening is caused by bulk motions and the ratio of the fractional ionizations for a pair of ions "$a, i$," "$b, j$" remains the same for all $U(x)$ along the sight line, then

$$\frac{\tau_{a,i}(\lambda)}{\tau_{b,j}(\lambda)} \propto \frac{N_{a,i}}{N_{b,j}} = \text{constant} . \quad (16)$$

Given the integral part of equation (15), which can be estimated from the unsaturated lines, we can easily calculate the column density for even saturated lines.

To test how accurately C II traces the distributions of other elements, we have studied the ionization properties of the warm H I gas assuming that it is embedded in an ionizing radiation field of given spectrum and intensity. The CLOUDY code (Ferland 1996) was used to compute the fractional ionization of ions $\Upsilon_{a,i}$ as a function of the ionization parameter $U$. For a given value of $n_{\rm ph}$, the fluctuation of $U$ along the line of sight represents the reciprocal hydrogen density. We consider two limiting types of radiation fields: a hard, QSO-dominated spectrum representative of the radiation field external to the $H_2$-bearing cloud at $z = 3$ (Haardt & Madau 1996); and a soft, starlight background given by Mathis, Mezger, & Panagia (1983). For the chosen ionizing spectra, $n_{\rm ph} = 2.2 \times 10^{-5}$ and $2.0 \times 10^{-6}$ cm$^{-3}$, respectively. Calculations were performed for metallicity $Z = 0.1\, Z_{\odot}$.

We found that most concordant with C II is the ion Si II, which traces C II over a rather wide range of $U$. This is illustrated in Figure 15, where the ratios $\Upsilon_{\rm Si\,II}/\Upsilon_{\rm C\,II}$ and $\Upsilon_{\rm Fe\,II}/\Upsilon_{\rm C\,II}$ (to stress the difference) are shown as functions of $U$. The displayed boundaries of $U$ correspond to $n_{\rm H} =$ 0.22–2.2 cm$^{-3}$ (hard ionizing spectrum) and $n_{\rm H} = 0.02$–$0.2$ cm$^{-3}$ (soft ionizing spectrum). Figure 15 shows that $\Upsilon_{\rm Si\,II}/\Upsilon_{\rm C\,II}$ is practically constant for both ionizing fields. The behavior of $\Upsilon_{\rm Fe\,II}/\Upsilon_{\rm C\,II}$ is, however, different: in both cases we may expect to observe nonsimilar profiles of the C II and Fe II lines.

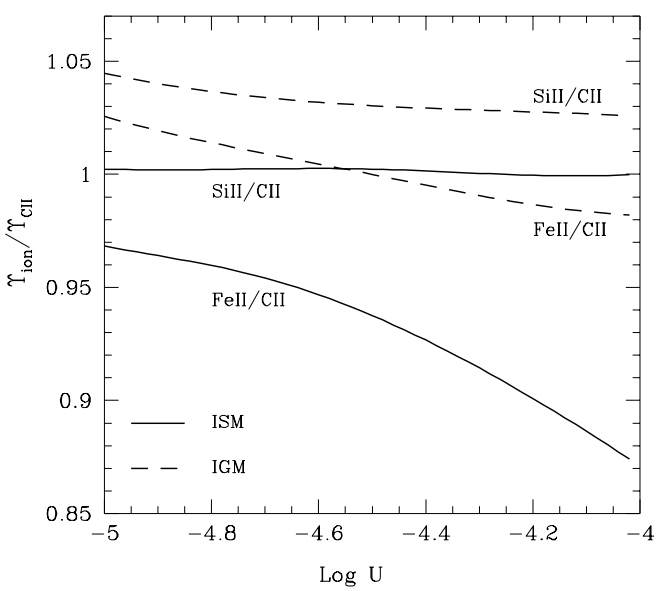


FIG. 15.—Fractional ionization ratios $\Upsilon_{\rm Si\,II}/\Upsilon_{\rm C\,II}$ and $\Upsilon_{\rm Fe\,II}/\Upsilon_{\rm C\,II}$ vs. the ionization parameter $U$ in the case of a soft, starlight background (*solid curves*) and a hard, QSO-dominated ionizing field (*dashed curves*). Similarity of the line profiles of a pair of ions requires the fractional ionization ratio to be constant for different $U$.

Thus, we can conclude from these calculations that independently of the background ionizing field the distribution of C II does trace the distribution of Si II in diffuse clouds ($0.1 \lesssim n_{\rm H} \lesssim 10$ cm$^{-3}$) and therefore we can use the unsaturated Si II profiles to measure $N$(C II) with a sufficiently high accuracy. In the present case we were able to describe with the same velocity distribution not only the C II and Si II lines but profiles of the other elements. This fact seems to justify the suggestion that the density fluctuations in the $H_2$ cloud are rather small and thus the derived $N$(C II) value can be considered as reliable.

## 4. DISCUSSION

We turn now to the question of the physical conditions in the $z_{\rm abs} = 3.025$ DLA. The measured column densities of metals and $H_2$ can be used to estimate the volumetric gas density and the intensity of the UV radiation field. We begin with the metal absorptions. Then we consider if the observed $H_2$ distribution over the excited rotational states can be described with metals in a self-consistent way. After that we compare the revealed [α-element/iron peak] ratio and abundances with those known from different DLA systems.

### 4.1. *Metal Absorption from the Ground and Excited States*

The absorption lines from the fine-structure levels of atoms and ions provide comprehensive information about the physical properties in the DLA systems (e.g., Bahcall & Wolf 1968; Silva & Viegas 2001). In equilibrium, the population ratio of the upper level $n_2$ to the lower level $n_1$, in ions with a doublet fine structure in the ground state, is given by

$$\frac{n_2}{n_1} \simeq \frac{Q_{1,2} + w_{1,2}}{A_{2,1}} , \quad (17)$$

where $w_{1,2}$ and $Q_{1,2}$ are the photon absorption and the collisional excitation rates, respectively, and $A_{2,1}$ is the radiative transition probability.

In the present analysis, we are interested mainly in the physical conditions in the gas where both the $H_2$ and the metal absorptions have been detected. We assume that this absorbing region is homogeneous and therefore the number density ratios are equal to the corresponding ratios of column densities, $n_2/n_1 = N_2/N_1$. We neglect fluorescence since this indirect excitation process has usually lower rates as compared to the direct collisional excitations and/or the IR radiative absorption rates. The radiative decay and the de-excitation rates are also ignored since in our case they have low efficiency.

In the main component of the $z_{\rm abs} = 3.025$ system the following quantities were estimated from the data listed in Table 3: $N$(H I) $= (2.521 \pm 0.035) \times 10^{20}$ cm$^{-2}$, $N$(C II) $= (5.05 \pm 0.28) \times 10^{15}$ cm$^{-2}$, C II*/C II $= (4.5 \pm 0.3) \times 10^{-3}$, C I/C II $< 8 \times 10^{-5}$, O I*/O I $< 3 \times 10^{-5}$, and Si II*/Si II $< 2 \times 10^{-3}$.

The ground state of the $C^+$ ion consists of two levels $2s^2 2p^2 P^0_{1/2,3/2}$ with the energy difference of $\Delta E = 91.32$ K and the spontaneous decay rate of $A_{2,1} = 2.291 \times 10^{-6}$ s$^{-1}$. The excited $J = 3/2$ level may be populated by collisions with electrons, $e^-$, hydrogen atoms, $H^0$, protons, $H^+$, and molecules, $H_2$. Among them the highest rate is found

for collisions with electrons: $Q^{e^-}_{1,2} \simeq 2 \times 10^{-7} n_e$ s$^{-1}$ in the range $10^2 < T_{\rm kin} < 10^3$ K (see, e.g., Fig. 3 in Silva & Viegas 2001). However, the electron density in H I regions comes mainly from the photoionization of carbon, $n_e \simeq ({\rm C/H}) n_{\rm H}$, which is approximately equal to $2 \times 10^{-5} n_{\rm H}$ for the $z_{\rm abs} = 3.025$ DLA. Then $Q^{e^-}{}_{1,2} \simeq 4 \times 10^{-12} n_{\rm H}$ s$^{-1}$ becomes lower than the $H^0$-$C^+$ collisional rate for the same temperature interval where $Q^{\rm H^0}_{1,2}$ is almost constant and equals $1.45 \times 10^{-9} n_{\rm H}$ s$^{-1}$ (Launay & Roueff 1977b). The rate of the photon absorption in the $z_{\rm abs} = 3.025$ DLA is mainly induced by the CMBR (Molaro et al. 2001a) and is equal to $w_{1,2} \simeq 1.1 \times 10^{-9}$ s$^{-1}$.

From equation (17) and taking the limiting values of the measured C II*/C II ratio, one obtains $n_{\rm H} \simeq 6$–$7$ cm$^{-3}$. The low limit of $n_{\rm H} \gtrsim 4$ cm$^{-3}$ stems from the analysis of the $H_2$ lines (see § 4.2).

To check the consistency of the estimated $n_{\rm H}$ with other metal absorption lines, we can use the upper limits to the column densities of O I* and Si II*. The equilibrium equation for the three-level system ($^3P_2$, $^3P_1$, $^3P_0$ states of $O^0$) can be written as (see Molaro et al. 2001b)

$$\frac{n_1}{n_0} \simeq \frac{(Q^{\rm H^0}_{0,1} + Q^{\rm H^0}_{0,2})}{A_{1,0}}, \qquad (18)$$

where the subscripts 0, 1, and 2 denote the ground (0) and excited (1, 2) levels, respectively. The spontaneous decay rate $A_{1,0} = 8.95 \times 10^{-5}$ s$^{-1}$, and the energy differences between the ground state and the corresponding fine-structure levels are $\Delta E_{0,1} = 228$ K and $\Delta E_{0,2} = 326$ K.

If $n_e$ is small, the rate coefficient for collisions with hydrogen atoms is dominating. At the kinetic temperature $T_{\rm kin} = 400$ K, we find from Launay & Roueff (1977a) $Q^{\rm H^0}_{0,1} = 1.65 \times 10^{-11} n_{\rm H}$ s$^{-1}$ and $Q^{\rm H^0}_{0,2} = 0.10 \times 10^{-11} n_{\rm H}$ s$^{-1}$. Then equation (18) yields $n_{\rm H} < 150$ cm$^{-3}$, which is consistent with the foregoing value.

The fine-structure level of the $Si^+$ ion ($^3P^0_{3/2}$) has an effective excitation temperature $\simeq 414$ K, which means that the estimated upper limit to $N$(Si II*) is less sensitive to low gas densities in this last case. Besides, absorption features produced by Si II* must come only from H II regions as argued by Spitzer & Jenkins (1975). The absence of the Si II* absorption might indicate that there is no dense H II gas region on the line of sight. This suggestion is also supported by the absence of the N II* $\lambda\lambda$1084.562 and 1084.580 lines in the $z_{\rm abs} = 3.025$ system. Both facts show that the C II* and C II absorptions arise predominantly in a warm H I gas in agreement with our model described in § 3.6.

### 4.2. $H_2$ *Distribution over the Rotational States*

We find no pronounced differences between the $H_2$ abundances in the $z_{\rm abs} = 3.025$ DLA system and in the Galactic diffuse clouds which have comparable H I column densities. The high excitation temperature in our system, $T_{\rm ex} = 825 \pm 110$ K, is also consistent with previous observations in the Galaxy. For instance, in a pioneer work by Spitzer & Cochran (1973) it has been shown that $T_{\rm ex} > 300$ K within diffuse interstellar clouds where the $H_2$ column density in the $J = 0$ rotational level $N(0) < 10^{15}$ cm$^{-2}$, and the temperature as high as 1100 K has been detected by Morton & Dinerstein (1976) toward $\zeta$ Pup.

It has been discussed in § 3.4 that the populations in the excited rotational states of $H_2$ cannot be supported only by collisions in a gas whose kinetic temperature is as high as 800 K. We calculated the $H_2$ collisional excitation rates by using the analytical approximations given in Shull & Beckwith (1982). The deduced rates are listed in columns (3) and (4) of Table 5 for $T_{\rm kin} = 400$ and 1000 K, respectively. In columns (5) and (6) we show, for comparison, the rates obtained in different models by Nishimura (1968) and Elitzur & Watson (1978). As noted by Shull & Beckwith (1982), the accuracy of the collisional excitation rates is not sufficiently high and different models may produce deviations of about 50%. The employed analytical fit to the $H^0$-$H_2$ excitation rates agrees with the Elitzur & Watson (1978) calculations to better than 25% but gives much lower values than the Nishimura (1968) rates. The radiative rates listed in column (2) were taken from Turner, Kirby-Docken, & Dalgarno (1977).

The collisional excitation of the $J = 3$ level is not expected to be effective in our case. Indeed, the $J = 2$ level has a longer radiative lifetime when compared with the $J = 3$ level ($t_{J=2} = 3.4 \times 10^{10}$ s and $t_{J=3} = 2.1 \times 10^9$ s, respectively), and therefore the $J = 2$ level is more sensitive to the collisional de-excitation. The critical density, $n^{\rm cr}_{\rm H} = A_{2\to0}/q_{2\to0}$, above which collisional de-excitation becomes important is $n^{\rm cr}_{\rm H} = 3.6$ cm$^{-3}$. Thus, $n_{\rm H} \gtrsim 4$ cm$^{-3}$ is required to maintain the observed $N(2)/N(0)$ ratio at $T_{\rm kin} = 400$ K. The absence of a fracture at lower $J$ in the graph log $[N(J)/g(J)]$ versus $E(J)$, shown in Figure 8, can be used to infer an upper limit for the gas density, $n_{\rm H} \lesssim 74$ cm$^{-3}$. Both limits are consistent with $n_{\rm H}$ estimated from the measured $N$(C II*)/$N$(C II) ratio.

Now we can set restrictions on the rate of photodissociation, $I$, in the $z_{\rm abs} = 3.025$ molecular cloud assuming that the $H_2$ molecules are formed on grains with rate $R$ and

TABLE 5

$H_2$ Transition Probabilities and Excitation Rate Coefficients for $\Delta J = 2$ Transitions between the First Five Rotational States

| $J$ (1) | $A_{J+2\to J}$[a] (s$^{-1}$) (2) | $q^{T=400{\rm K}}_{J\to J+2}$[b] (cm$^3$ s$^{-1}$) (3) | $q^{T=1000{\rm K}}_{J\to J+2}$[b] (cm$^3$ s$^{-1}$) (4) | $q^{T=1000{\rm K}}_{J\to J+2}$[c] (cm$^3$ s$^{-1}$) (5) | $q^{T=1000{\rm K}}_{J\to J+2}$[d] (cm$^3$ s$^{-1}$) (6) |
|---|---|---|---|---|---|
| 0..... | 2.94E−11 | 1.14E−11 | 6.44E−11 | 4.82E−11 | 1.27E−10 |
| 1..... | 4.76E−10 | 1.79E−12 | 1.60E−11 | ... | 4.07E−11 |
| 2..... | 2.76E−9 | 5.16E−13 | 7.35E−12 | 6.70E−12 | 1.78E−11 |
| 3..... | 9.84E−9 | 1.76E−13 | 4.02E−12 | ... | 8.33E−12 |

[a] Turner et al. 1977.
[b] This paper.
[c] Elitzur & Watson 1978.
[d] Nishimura 1968.

partly destroyed through the fluorescence process. In equilibrium, the fractional molecular abundance is given by (Jura 1974)

$$f_{H_2} \simeq \frac{2Rn_H}{I} . \quad (19)$$

To estimate the rate of formation of $H_2$, we use the approximation from Black & Dalgarno (1977):

$$R \simeq 10^{-6} T_{kin}^{0.5} n_H n_d \text{ cm}^3 \text{ s}^{-1} . \quad (20)$$

Here the number density of dust grains, $n_d$, is related to the total hydrogen density, $n$, through

$$n_d = 10^{-12} n = 10^{-12}(n_H + 2n_{H_2}) , \quad (21)$$

which is the usual relation for the interstellar diffuse clouds.

Then, accounting for the dust-to-gas ratio $\tilde{k} \simeq 0.05$ (see § 3.5) and the fact that $n_{H_2} \ll n_H$ in the $z_{abs} = 3.025$ cloud, we find

$$R \simeq 10^{-18} T_{kin}^{0.5} \tilde{k} n_H^2 \simeq 5 \times 10^{-20} T_{kin}^{0.5} n_H^2 \text{ cm}^3 \text{ s}^{-1} . \quad (22)$$

Then for $T_{kin} = 400$ K, $H_2$ forms at a rate $R \simeq 1.0 \times 10^{-18} n_H^2$ cm$^3$ s$^{-1}$.

This value of $R$ will be consistent with the upper limit found by Jura (1974) in the Galactic ISM, $R_G \lesssim 2 \times 10^{-16}$ cm$^3$ s$^{-1}$, if $n_H \lesssim 14$ cm$^{-3}$ at $z_{abs} = 3.025$. By this we confine $n_H$ in the interval $4 \lesssim n_H \lesssim 14$ cm$^{-3}$, which provides a self-consistency between the observed $N(2)/N(0)$ ratio and the maximum formation rate of $H_2$ under the condition that the physical properties of the dust grains in the Milky Way and at $z_{abs} = 3.025$ are similar.

Since the molecular hydrogen fractional abundance in the main component of the $z_{abs} = 3.025$ absorber is $f_{H_2} = (3.3 \pm 0.2) \times 10^{-6}$, cloud parameters $n_H \simeq 6$ cm$^{-3}$ and $T_{kin} = 400$ K will yield $I \simeq 2 \times 10^{-10}$ s$^{-1}$, which agrees well with the values measured in the interstellar clouds containing optically thin $H_2$: $0.5 \times 10^{-10} \leq I_G \leq 16.0 \times 10^{-10}$ s$^{-1}$ (Jura 1975a). Thus, the radiation field in the $z_{abs} = 3.025$ cloud is quite comparable with those measured in transparent interstellar clouds in the Milky Way.

We now evaluate the total hydrogen density, $n_H$, the photoabsorption rate, $\beta_0$, and the steady state production rate of molecular hydrogen, $R$, from the relative population of the different rotational levels of $H_2$. Our analysis is, in general, the same as described by Spitzer & Zweibel (1974) and Jura (1974, 1975a, 1975b). However, we recalculated the formation efficiency coefficients $\varepsilon_4$ and $\varepsilon_5$ for the $J = 4$ and 5 levels including upper rotational levels with a cutoff above $J_{max} = 15$. These coefficients were calculated from the Boltzmann distribution of molecules formed upon grain surfaces with an effective temperature, $T_f$ (for details see Black & Dalgarno 1976). Since a newly formed molecule quickly cascades to the ground vibrational level, we assume that the newly formed molecules populate the ($v = 0$, $J = 4$) and ($v = 0$, $J = 5$) levels. It is usually assumed that molecules are formed at $T_f \simeq 17{,}400$ K, which is the temperature equivalent of the binding energy of $H_2$ distributed statistically among the rotation vibration levels upon formation (e.g., Spitzer & Zweibel 1974). Then we find $\varepsilon_4 = 0.21$ and $\varepsilon_5 = 0.65$ (cf. $\varepsilon_4 = 0.19$ and $\varepsilon_5 = 0.44$ from Jura 1975b).

The concentrations of $H_2$ in the $J = 4$ and 5 levels may be approximately estimated from the statistical equilibrium equations

$$A_{4+K,2+K} n_{4+K} = \varepsilon_{4+K} R n_H^2 + \beta_0 \sum_{J'} p_{4+K,J'} n_{J'} , \quad (23)$$

where $J' = K$, $K + 2$, and $K + 4$ and $K = 0$ or 1 for $J = 4$ or 5, respectively.

In these equations, the pumping efficiency coefficients $p_{i,j}$ are taken from Jura (1975a). The quantity $p_{i,j}$ shows the probability (averaged over the different Lyman and Werner bands) that photoabsorption from the $j$th rotational level will lead to the population of the $i$th rotational level in the ground $v = 0$ vibrational state.

From equation (23) we can calculate $Rn_H$ using the measured $N(4)/N(H)$ and $N(5)/N(H)$ ratios. It gives $Rn_H \simeq 3 \times 10^{-16}$ s$^{-1}$. If we take $R \simeq 5 \times 10^{-17}$ cm$^3$ s$^{-1}$ from Spitzer & Cochran (1973), then $n_H \simeq 6$ cm$^{-3}$. Now the $H_2$ destruction rate can be estimated from equation (19), which gives again $I \simeq 2 \times 10^{-10}$ s$^{-1}$ as in the foregoing estimations. If $I \simeq 0.11\beta_0$ (Jura 1974), then the rate of photoabsorption is $\beta_0 \simeq 2 \times 10^{-9}$ s$^{-1}$. On the other hand, the average $\beta_0$ for the intergalactic UV background at $z \simeq 3$ is about $2 \times 10^{-12}$ s$^{-1}$ (Srianand & Petitjean 1998), while the Milky Way interstellar radiation field value is in the interval $5 \times 10^{-10} \leq \beta_0 \leq 1.6 \times 10^{-8}$ s$^{-1}$ (Jura 1975a). Thus, our measurements show a close similarity with the average characteristics of the UV field found in the Milky Way.

For the neutral hydrogen column density $N(\text{H I}) \simeq 2.5 \times 10^{20}$ cm$^{-2}$ and $n_H \simeq 6$ cm$^{-3}$, the linear size of the $H_2$-bearing cloud along the line of sight is equal to $D \simeq 14$ pc, which yields a mass of $M \simeq 0.5 D^3 n_H m_H \simeq 200\ M_\odot$, assuming spherical geometry.

### 4.3. [α-Element/Iron Peak] Ratios

The elemental column densities obtained following the procedure described in §§ 3.5 and 3.6 together with the relative abundances are summarized in Table 4. Among the elements belonging to the iron peak group, Zn is a good indicator of the absolute metal abundance in the system, since Zn is known to be essentially undepleted in the ISM (Pettini et al. 1999). Measurements of Zn in high-redshift systems have been proven to be very challenging since the Zn II resonance lines fall at wavelengths greater than 8000 Å where spectrograph and CCD efficiency decreases while sky emissivity increases. The Zn measurement presented here and that in the DLA at $z_{abs} = 3.39$ toward Q0000−2621 are the only ones obtained for systems with $z \geq 3$. The derived $[\text{Zn/H}] = -1.50 \pm 0.05$ is in line with the bulk of [Zn/H] measurements found in the redshift interval $2 < z < 2.5$ although higher by 0.6 dex than that of the DLA at $z_{abs} = 3.39$ toward Q0000−2621, confirming the presence of significant spread in absolute abundance in DLA with comparable redshifts. The straight mean of the Zn measurements in the redshift interval $2 \leq z \leq 3$ is $[\text{Zn/H}] \approx -1.2$ and does not differ from the column density–weighted mean for the same redshift interval (Vladilo et al. 2000). This new measurement therefore supports the general metallicity behavior, characterized by the intrinsic spread for a given redshift and by a mild trend of increasing abundance with the decreasing redshift if not a lack of evolution when the hydrogen column density–weighted mean is considered.

As described in § 3.6, our model keeps the constant ratio between the matching components. With this condition imposed, we cannot account for different chemical abundances or the presence of different dust pattern depletion

among the components of the system. It may be possible that a contribution from warmer gas or different dust depletion is responsible for the observed difference in profile shapes of Fe II and other ions.

Only recently did it become possible to measure oxygen with an acceptable accuracy using the fainter O I lines falling in the Ly$\alpha$ forest instead of the always strongly saturated O I $\lambda$1302 transition (Lopez et al. 1999; Molaro et al. 2000; Dessauges-Zavadsky et al. 2001). In the present paper the O abundance is derived from the set of 11 O I lines used either for direct fitting or just for the consistency test.

The [O/Zn] is the most informative ratio to trace back the kind of chemical evolution of the absorber. Both elements show little affinity with dust grains and are good representatives of $\alpha$-chain and iron peak elements, respectively. If the system is in the early stages of chemical evolution, the relative abundances should reflect the yields of Type II supernovae characterized by the enhancement of $\alpha$-elements. In fact, it was rather surprising to find little evidence for this enhancement when elements such as S and Si, once corrected by dust, were used in combination with Zn (Centurión et al. 2000; Vladilo 1998), and the ratio [O/Zn] = 0.1 has been measured in the DLA toward Q0000−2621 (Molaro et al. 2001b).

The ratio [O/Zn] = 0.68 ± 0.08, found here, represents the first clear-cut evidence for a genuine enhancement of the $\alpha$-elements comparable to that observed in the metal-poor stellar population of the Milky Way (Israelian et al. 2001). The oxygen result is also supported by the other $\alpha$-elements we have been able to measure, namely, [Ar/Zn] = 0.34 ± 0.07, [Si/Zn] = 0.56 ± 0.06, and [S/Zn] = 0.41 ± 0.08 (if we take log [$N$(S II)] = 14.73 ± 0.01 cm$^{-2}$ from Prochaska & Wolfe 1999). Argon abundance is slightly below the values obtained from the other $\alpha$-elements, but this is not surprising since Ar is sensitive to photoionization effects and shows in the Galaxy even larger depletion factors (Sofia & Jenkins 1998).

All results available at present allow us to conclude that the DLA systems probably comprise a mix of chemical abundance pattern with both low and *standard* $\alpha$-element enhancement. It is not clear at the moment if this reflects the different enrichment histories or just the same type of galaxies caught at different stages of their chemical evolution. It is interesting to note that estimated in the $H_2$-bearing cloud the ratio (Ar/O) = −2.65 is comparable to that observed in the DLA toward Q0000−2621, (Ar/O) = −2.25 (Molaro et al. 2001b), in particular when allowing for a small degree of Ar photoionization. As argued by Henry & Worthey (1999), the similarity of these ratios in a variety of galactic systems from the Milky Way to blue compact galaxies strengthens the case for the existence of a universal initial mass function.

It is commonly assumed that nitrogen is mostly produced by the intermediate massive stars (Henry, Edmunds, & Köppen 2000). In DLA systems, N shows a scatter well in excess of observational uncertainties which has been interpreted as being due to the delayed release of N compared to O (Centurión et al. 1998). Our value in the "[O/H]-[N/O]" plane has coordinates [O/H] = −0.82 and [N/O] = −0.84 and falls close to the line for a pure secondary origin for N (see Fig. 8 in Centurión et al. 1998). If intermediate massive stars had not yet time to evolve and to contribute to the N enrichment, then this sets an upper limit of approximately $10^8$ yr to the evolutionary age of the $z_{abs} = 3.025$ system. The young age of the system under study is also consistent with the observed $\alpha$-element enhancement.

Phosphorus has been measured in the DLA toward Q0000−2621 (Molaro et al. 2001b) and toward Q1759+7539 (Outram, Chaffee, & Carswell 1999). P cannot be measured in halo stars, and thus the DLA systems provide a unique astrophysical site where this element can be measured in low-metallicity environments. Our determination is based only on the P II $\lambda$963.8 line and may be slightly overestimated as a result of H I contamination. We have here the mean value of [P/Si] $\approx$ −0.2, which suggests the presence of a moderately odd $Z$/even $Z$ effect which is a common feature in all P measurements in DLA systems so far.

## 5. CONCLUSIONS

The main results of this paper are as follows:

1. In the high-resolution UVES spectrum of the quasar Q0347−3819 we have identified over 80 absorption features with the Lyman and Werner lines arising from the $J = 0$–5 rotational levels of the ground electronic vibrational state of $H_2$. These lines belong to the $z_{abs} = 3.025$ DLA system.

2. The application of the standard Voigt fitting analysis to the main subcomponent at $z_{H_2} = 3.024855 \pm 0.000005$ gives the total $H_2$ column density of $N(H_2) = (4.10 \pm 0.21) \times 10^{14}$ cm$^{-2}$ and the Doppler width $b_{H_2} = 2.80 \pm 0.45$ km s$^{-1}$. The kinetic gas temperature is less than 430 K.

3. The fractional abundance of $H_2$ in the main component is equal to $f_{H_2} = (3.3 \pm 0.2) \times 10^{-6}$, while being compared to the total H I column density it yields $f_{H_2} = (1.94 \pm 0.10) \times 10^{-6}$. These values are similar to those observed in the ISM diffuse clouds with low color excesses, $E(B-V) < 0.1$. Using the total hydrogen column density in the main component $N$(H I) $\simeq 2.5 \times 10^{20}$ cm$^{-2}$ and the approximate relationship $N(H) \simeq 7.5 \times 10^{21} E(B-V)$ cm$^{-2}$ mag$^{-1}$, which assumes that the gas and dust grains are uniformly mixed (Spitzer & Jenkins 1975), we obtain $E(B-V) \simeq 0.03$ mag in the $H_2$-bearing cloud. For the second strong component with $N$(H I) $\simeq 1.5 \times 10^{20}$ cm$^{-2}$ at $\Delta v \simeq -17$ km s$^{-1}$ we set a very low limit to $f_{H_2} < 3.3 \times 10^{-9}$ (3 $\sigma$). The $z_{abs} = 3.025$ system is not a homogeneous cloud but rather a mixture of cold and warm gas.

4. The total column densities in the ortho- and para-$H_2$ states yield the ratio $N_{ortho}/N_{para} = 3.1 \pm 0.3$, which is close to 3:1 expected from the hot $H_2$ formation upon grain surfaces. Similar ratios of 2.4 ± 0.9 and 3.1 ± 0.8 are estimated at $z_{abs} = 2.33771$ and 2.8112 toward Q1232+0815 and Q0528−250 from the published data by Srianand et al. (2000) and Srianand & Petitjean (1998), respectively. These ratios are, however, higher than the "freezeout" ortho-$H_2$:para-$H_2$ = 1:4 predicted for the early universe at $z < 20$ (Flower & Pineau des Forêts 2000). It appears that $H_2$ detected in these three DLA systems has undergone a reforming phase in the period between $z \simeq 20$ and 3 ($\Delta t \simeq 2$ Gyr).

5. We found that the population of the low rotational levels can be represented by a single excitation temperature of $T_{ex} = 825 \pm 110$ K. Such high $T_{ex}$ agrees well with the results by Spitzer & Cochran (1973), who showed that $T_{ex} > 300$ K within diffuse clouds which have $N(J = 0) < 10^{15}$ cm$^{-2}$, as it is in our case.

6. From the measured [Cr/H] and [Zn/H] ratios we cal-

culated the gas-to-dust ratio $\tilde{k} = 0.032 \pm 0.005$ in the whole $z_{abs} = 3.025$ system (the ratio [Cr/Zn] is usually used to indicate the presence of dust in DLA systems). The derived $H_2$ fractional abundance fits well in the linear relation between $\log f_{H_2}$ and [Cr/Zn], supporting our previously obtained results for other DLA systems (Levshakov et al. 2000b).

7. From the observed population ratios of $H_2$ in different rotational states and the C II*/C II ratio we inferred the hydrogen number density $n_H$ in the $H_2$-bearing cloud $n_H \simeq 6$ cm$^{-3}$ and the cloud dimension along the line of sight $D \simeq 14$ pc, which gives $M \simeq 200\, M_\odot$.

8. From the relative populations of $H_2$ in the $J = 4$ and 5 rotational levels we estimated the rate of photodestruction $I \simeq 2 \times 10^{-10}$ s$^{-1}$. The photoabsorption rate, $\beta_0 \simeq I/0.11$, is thus equal to $\beta_0 \simeq 2 \times 10^{-9}$ s$^{-1}$. Taking into account that the Milky Way interstellar radiation field value is in the interval $5 \times 10^{-10} \leq \beta_0 \leq 1.6 \times 10^{-8}$ s$^{-1}$ (Jura 1975a), we conclude that the UV radiation fields in the $z_{abs} = 3.025$ absorbing cloud and in the Galactic ISM are very much alike. We also found that the formation rate of $H_2$ upon grain surfaces, $Rn_H \simeq 3 \times 10^{-16}$ s$^{-1}$, is similar to that found in the Galaxy by Jura (1975a).

9. The metal abundances from the $z_{abs} = 3.025$ DLA reveal a pronounced [$\alpha$-element/iron peak] enhancement with [O, Si/Zn] $= 0.6 \pm 0.1$ at the 6 $\sigma$ confidence level, the first time that this abundance pattern is unambiguously identified in a DLA system. The same order of magnitude enrichment of $\alpha$-chain elements has been observed in Galactic metal-poor stars. The measured [N/O] ratio implies the chemical history age of this DLA of $\lesssim 10^8$ yr.

10. The analysis of the metal profiles combined with the H + D Lyman series lines yields a new estimation of the hydrogen isotopic ratio D/H $= (3.75 \pm 0.25) \times 10^{-5}$ in this DLA. It implies for the baryon-to-photon ratio, $\eta$, a value in the interval $4.37 \times 10^{-10} \lesssim \eta \lesssim 5.32 \times 10^{-10}$ and the present-day baryon density $\Omega_b h^2 \simeq 0.016$–$0.020$, which is in good agreement with a new analysis of the BOOMERANG experiment yielding $\Omega_b h^2 = 0.021 \pm 0.003$ (Netterfield et al. 2001).

S. A. L. gratefully acknowledges the hospitality of the European Southern Observatory (Garching), Osservatorio Astronomico di Trieste, and the National Astronomical Observatory of Japan (Mitaka) where this work was performed. We also thank A. Wolfe and J. X. Prochaska for making available the calibrated Keck/HIRES spectrum of Q0347−3819 and I. I. Agafonova for many valuable comments on data analysis. We are greatly indebted to our referee for noting a shortcoming in the pipeline software and for helpful comments. The work of S. A. L. is supported in part by RFBR grant 00-02-16007.

## APPENDIX A

## CORRELATED MEASUREMENTS

In order to evaluate the uncertainties in the derived physical parameters, one must know the standard errors, $\sigma_j$, for all the data points. These errors, computed through the UVES data reduction pipeline (Ballester et al. 2000), are not, however, statistically independent. The pipeline data resampling to constant wavelength bins introduces a correlation between the data point values. Besides, the resampling procedure can change statistical properties of the noise (e.g., the simplest linear interpolation scheme smooths the random noise since the uncertainty of the data point value halfway between two measurements is less than that for the real detector amplitudes at the limiting points).

Data point correlation is clearly seen in Figure 7, where the sequences of points at the continuum level (e.g., panels L2-0R0 and L2-0P3) show that neighboring points differ from each other by less than $\sigma_j$ (for the data shown in Fig. 7, the correlation coefficient $r \simeq 0.77$). The correlation length, $\xi$, of about 1.5 bins can be deduced from the analysis of the autocorrelation function[11] (ACF) of the intensity fluctuations in the continuum windows free from absorption-line features. This ACF is shown by the histogram in Figure 16*a*, where an exponential correlation function $f(\Delta n) = \exp(-\Delta n/\xi)$ of the simplest data model, the first-order autoregression (the Markov process), is overdrawn by the smooth curve (here $\Delta n$ is the scale shift).

The correlated data make the standard $\Delta\chi^2$ calculation of parameter confidence intervals questionable. To investigate this point, we performed the following Monte Carlo (MC) analysis in combination with the least-squares method.

It is well known that the least-squares method (LSM) is computationally equivalent to the $\chi^2$ minimization (e.g., Meyer 1975). It is also known that the LSM is an unbiased and minimum variance estimator (Gauss-Markov theorem) irrespective of the distribution of the measurements including correlated data as well (Aitken 1934). Therefore, in the MC analysis, we used the best-fitting parameters (the parameter vector $\hat{\theta}$; see § 3.6) found by means of the standard $\chi^2$ minimization and calculated uncertainties of the $\hat{\theta}$-components in the vicinity of the global minimum of the objective function by using the MC procedure.

Our computational MC procedure consists of the following steps:

1. A simulation box in the parameter space is specified by fixing the parameter boundaries $\hat{\theta}_i(1 - \beta) < \theta_i < \hat{\theta}_i(1 + \beta)$; in our case $\beta = 0.3$.

2. Initial guess $\theta^{(0)}$ is chosen arbitrary within the simulation box.

3. A random realization of the "observational" points is generated in the following way: the $j$th data point value is altered with a probability $P$ by means of the relation

$$\mathscr{F}_j^{\rm rnd} = \mathscr{F}_j^{\rm obs} + \sigma_j g \ ,$$

[11] The ACF is defined, e.g., in Bendat & Piersol (1971).

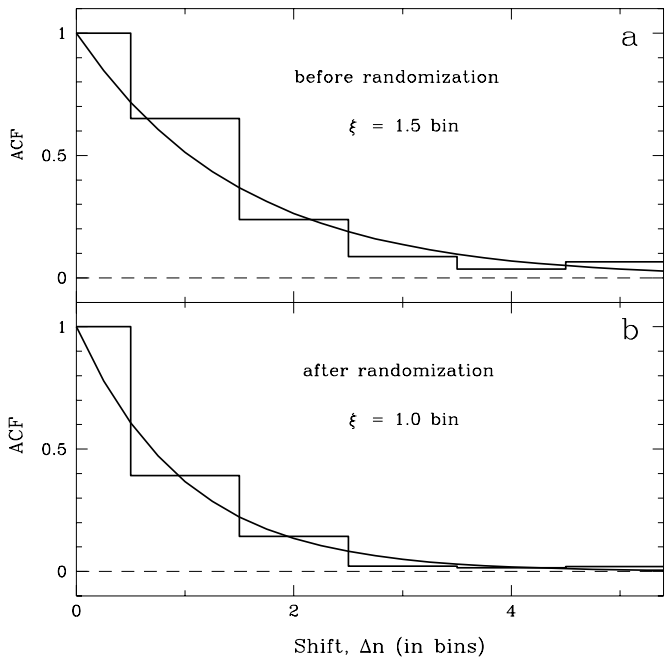


FIG. 16.—ACFs of the intensity fluctuations in the continuum between 6790 and 6820 Å in the UVES spectrum of Q0347−3819 before and after randomization (*histograms* in panels [*a*] and [*b*], respectively). The smooth curves show the ACFs of the first-order autoregression process with correlation lengths indicated by $\xi$ (see text for more details).

where $g$ is a random normal variable with zero mean and unit dispersion and $\mathscr{F}_j^{\rm obs}$ is the normalized observational intensity[12] in the $j$th bin ($j = 1, 2, \ldots, \mathscr{N}$, with $\mathscr{N}$ being the total number of data points).

4. Objective function is minimized and all solutions with $\chi^2 < 1.10$ are collected.

5. The whole procedure is repeated many times to collect a representative sample (i.e., the number of measurements $\mathscr{K} > 30$). Then the sample mean and standard deviation are calculated.

To compare both $\Delta\chi^2$ and MC results, we carried out the MC procedure for the $b$ parameter and the $H_2$ abundances at different $J$ levels. A total of 19 $H_2$ lines (L3-0R0, L7-0R0, L1-0P1, L3-0P1, L14-0P1, W0-0R2, W0-0Q2, L3-0R2, L4-0R2, L5-0R2, L2-0R3, L2-0P3, L3-0P3, L4-0R3, L15-0R3, L5-0R4, L8-0P4, L7-0P5, L12-0R5; see Figs. 5 and 6) have been chosen and fitted simultaneously with the individual Gaussian profiles. The obtained estimations (for $\mathscr{N} = 177$ and $\mathscr{K} = 181$) summarized in Table 6 show that in this case $\Delta\chi^2$ yields practically the same mean values but systematically higher standard deviations. Since statistical properties of the noise are not exactly known, we use in the present paper the most conservative $\Delta\chi^2$ estimations of the standard deviations and the mean values.

## APPENDIX B

## METAL SYSTEMS TOWARD Q0347−3819

We have thoroughly investigated all possible coincidences of $H_2$, H I, D I, and metal absorption features from the $z_{\rm abs} = 3.025$ DLA system with metal absorptions from other systems observed toward Q0347−3819. Positions of the found

[12] This randomization decreases the correlation between consecutive bins but increases the noise. For instance, if $P = 0.7$, the correlation length equals $\xi \simeq 1.0$ bin (see Fig. 16*b*), but the noise level is about a factor of $\sqrt{2}$ higher.

TABLE 6

COMPARISON OF THE MEAN VALUES AND THE STANDARD DEVIATIONS ESTIMATED BY THE MONTE CARLO (MC) AND $\Delta\chi^2$ METHODS IN CASE OF CORRELATED MEASUREMENTS

| Parameter, $x$ | $\langle x\rangle_{\rm MC}$ | $\sigma_{\rm MC}$ | $\langle x\rangle_{\Delta\chi^2}$ | $\sigma_{\Delta\chi^2}$ |
|---|---|---|---|---|
| $b$ (km s$^{-1}$) ..... | 3.04 | 0.29 | 2.80 | 0.45 |
| $N(J = 0)$ (cm$^{-2}$)..... | 1.90E13 | 0.29E13 | 1.90E13 | 0.35E13 |
| $N(J = 1)$ (cm$^{-2}$)..... | 1.84E14 | 0.13E14 | 1.60E14 | 0.18E14 |
| $N(J = 2)$ (cm$^{-2}$)..... | 5.39E13 | 0.28E13 | 5.40E13 | 0.35E13 |
| $N(J = 3)$ (cm$^{-2}$)..... | 1.24E14 | 0.07E14 | 1.22E14 | 0.05E14 |
| $N(J = 4)$ (cm$^{-2}$)..... | 2.35E13 | 0.44E13 | 2.60E13 | 0.43E13 |
| $N(J = 5)$ (cm$^{-2}$)..... | 2.90E13 | 0.53E13 | 2.90E13 | 0.70E13 |

NOTE.—The $H_2$ column densities at different $J$ levels and the corresponding broadening parameter $b$ are listed in the first column.

blends are indicated in Figures 5, 6, 10, and 11. The strongest systems detected in the spectral ranges $\lambda = 3680$–$4880$ Å, 4880–6730 Å (this portion of the spectrum obtained at the Keck telescope was kindly shared with us by A. M. Wolfe & J. X. Prochaska), 6730–8520 Å, and 8685–10000 Å are listed below. Since almost all identified metal profiles exhibit complex structures, the quoted redshifts are the ones of the strongest components or the average redshifts in the cases in which the components are not well separated. In cases in which the hydrogen Ly$\alpha$ line lies outside the observable spectral range, we consider a doublet of absorption lines caused by the same ion as an individual metal system if the lines show identical profile shapes. The identifications made in the $z_{\rm abs} = 3.025$ DLA are not included in the list. Possible blends are shown in parentheses.

$z_1 = 0.000019$: Ca II $\lambda\lambda$3934, 3969 (+ W1-0R2).
$z_2 = 1.4579$: Mg I $\lambda$2852; Mg II $\lambda\lambda$2796, 2803; Al II $\lambda$1670; Al III $\lambda$1854; Si II $\lambda\lambda$1526, 1808; Fe II $\lambda\lambda$1608, 2260, 2344, 2374, 2382, 2586, 2600.
$z_3 = 1.5159$: C IV $\lambda\lambda$1548, 1550.
$z_4 = 1.5263$: Mg II $\lambda\lambda$2796, 2803; Si II $\lambda\lambda$1526 (+ Ly$\gamma$ $z_{15}$), 1808; Fe II $\lambda\lambda$2344, 2382, 2600.
$z_5 = 1.6768$: C IV $\lambda\lambda$1548, 1550.
$z_6 = 2.2140$: Ly$\alpha$; C II $\lambda$1334; C IV $\lambda\lambda$1548, 1550; O I $\lambda$1302; Mg II $\lambda\lambda$2796, 2803; Al II $\lambda$1670; Al III $\lambda$1854; Si II $\lambda\lambda$1190 (+ W3-0Q3), 1193, 1260; Si III $\lambda$1206; Si IV $\lambda\lambda$1393, 1402; Fe II $\lambda\lambda$1608, 2344, 2374, 2382, 2586, 2600.
$z_7 = 2.3932$: Ly$\alpha$ (+ Ly$\beta$ DLA); C IV $\lambda\lambda$1548, 1550.
$z_8 = 2.4344$: Ly$\alpha$; C IV $\lambda\lambda$1548, 1550.
$z_9 = 2.5371$: Ly$\alpha$; C II $\lambda$1334; C IV $\lambda\lambda$1548, 1550; Al II $\lambda$1670; Si II $\lambda$1260; Si IV $\lambda$1393.
$z_{10} = 2.6504$: Ly$\alpha$; C IV $\lambda\lambda$1548, 1550; Si III $\lambda$1206; Si IV $\lambda\lambda$1393, 1402.
$z_{11} = 2.6526$: Ly$\alpha$; C IV $\lambda\lambda$1548, 1550; Si III $\lambda$1206; Si IV $\lambda\lambda$1393, 1402.
$z_{12} = 2.8102$: Ly$\alpha$; C II $\lambda$1334; Si II $\lambda\lambda$1190, 1193, 1260 (+ Si II $\lambda$1193 DLA); Si IV $\lambda\lambda$1393, 1402.
$z_{13} = 2.8483$: Ly$\alpha$, Ly$\beta$ (+ Ly$\gamma$ $z_{19}$); C III $\lambda$977; C IV $\lambda\lambda$1548, 1550.
$z_{14} = 2.8992$: Ly$\alpha$, Ly$\beta$, Ly$\gamma$, Ly$\delta$; C IV $\lambda\lambda$1548, 1550; C III $\lambda$977; Si III $\lambda$1206; Si IV $\lambda\lambda$1393, 1402.
$z_{15} = 2.9617$: Ly$\alpha$, Ly$\beta$, Ly$\gamma$, Ly$\delta$; C III $\lambda$977; C IV $\lambda\lambda$1548, 1550 (+ Si II $\lambda$1526 DLA); N II $\lambda$1083; N III $\lambda$989; Al III $\lambda$1854; Si II $\lambda$1190; Si III $\lambda$1206.
$z_{16} = 2.9659$: Ly$\alpha$, Ly$\beta$, Ly$\gamma$ (+ Si II $\lambda$1526 $z_4$), Ly$\delta$, Ly$\varepsilon$; C III $\lambda$977; C IV $\lambda$1548; N III $\lambda$989 (+ L11-0P2); Si III $\lambda$1206.
$z_{17} = 2.9792$: Ly$\alpha$, Ly$\beta$, Ly$\gamma$; C II $\lambda$1036 (+ Ly$\beta$ DLA); C III $\lambda$977; C IV $\lambda\lambda$1548, 1550.
$z_{18} = 3.0217$: Ly$\alpha$ (+ Ly$\alpha$ DLA); C III $\lambda$977 (+ O I $\lambda$976 DLA); C IV $\lambda\lambda$1548, 1550; N II $\lambda$1083; N III $\lambda$989; Si IV $\lambda\lambda$1393, 1402.
$z_{19} = 3.0632$: Ly$\alpha$, Ly$\beta$, Ly$\gamma$ (+ Ly$\beta$ $z_{13}$), Ly$\delta$ (+ N III $\lambda$989 $z_{14}$); C III $\lambda$977; C IV $\lambda\lambda$1548, 1550.

## REFERENCES


Abgrall, H., & Roueff, E. 1989, A&AS, 79, 313
Aitken, A. C. 1934, Proc. R. Soc. Edinburg A, 55, 42
Andreani, P., Cimatti, A., Loinard, L., & Röttgering, H. 2000, A&A, 354, L1
Bahcall, J. N., & Wolf, R. A. 1968, ApJ, 152, 701
Ballester, P., Modigliani, A., Boitquin, O., Cristiani, S., Hanuschik, R., Kaufer, A., & Wolf, S. 2000, Messenger, 101, 31
Barvainis, R., Maloney, P., Alloin, D., & Antonucci, R. 1997, ApJ, 484, 695
Bendat, J. S., & Piersol, A. G. 1971, Random Data: Analysis and Measurement Procedures (New York: Wiley)
Bergeson, S. D., & Lawler, J. E. 1993, ApJ, 408, 382
Black, J. H., & Dalgarno, A. 1976, ApJ, 203, 132
———. 1977, ApJS, 34, 405
Brown , R. L., & vanden Bout, P. A. 1992, ApJ, 397, L19
Burles, S., Nollett, K. M., Truran, J. N., & Turner, M. S. 1999, Phys. Rev. Lett., 82, 4176
Cardelli, J. A., & Savage, B. D. 1995, ApJ, 452, 275
Carilli, C. L., Menten, K. M., & Yun, M. S. 1999, ApJ, 521, L25
Carruthers, G. 1970, ApJ, 161, L81
Centurión, M., Bonifacio, P., Molaro, P., & Vladilo, G. 1998, ApJ, 509, 620
———. 2000, ApJ, 536, 540
Charro, E., & Martín, I. 2000, ApJS, 126, 551
de Boer, K. S., Richter, P., Bomans, D. J., Heithausen, A., & Koornneef, J. 1998, A&A, 338, L5
Dessauges-Zavadsky, M., D'Odorico, S., McMahon, R. G., Molaro, P., Ledoux, C., Péroux, C., & Storrie-Lombardi, L. J. 2001, A&A, 370, 426
D'Odorico, S., Cristiani, S., Dekker, H., Hill, V., Kaufer, A., Kim, T., & Primas, F. 2000, Proc. SPIE, 4005, 121
D'Odorico, S., Dessauges-Zavadsky, M., & Molaro, P. 2001, A&A, 368, L21 (DDM01)
Downes, D., Neri, R., Wiklind, T., Wilner, D. J., & Shaver, P. A. 1999, ApJ, 513, L1
Elitzur, M., & Watson, W. D. 1978, A&A, 70, 443
Federman, S. R., Beideck, D. J., Schectman, R. M., & York, D. G. 1992, ApJ, 401, 367
Ferland, G. J. 1996, A Brief Introduction to CLOUDY (Internal Rep.; Lexington: Univ. Kentucky)
Field, G. B., Sommerville, W. B., & Dressler, K. 1966, ARA&A, 4, 207
Flower, D. R., & Pineau des Forêts, G. 2000, MNRAS, 316, 901
Foltz, C. B., Chaffee, F. H., & Black, J. H. 1988, ApJ, 324, 267
Frayer, D. T., et al. 1999, ApJ, 514, L13
Fuller, T. M., & Couchman, H. M. P. 2000, ApJ, 544, 6
Galli, D., & Palla, F. 1998, A&A, 335, 403
Ge, J., & Bechtold, J. 1997, ApJ, 477, L73
———. 1999, in ASP Conf. Ser. 156, Highly Redshifted Radio Lines, ed. C. L. Carilli, S. J. E. Radford, K. M. Menten, & G. I. Langston (San Francisco: ASP), 121
Ge, J., Bechtold, J., & Kulkarni, V. P. 2001, ApJ, 547, L1
Gould, R. J., & Salpeter, E. E. 1963, ApJ, 138, 393
Grevesse, N., & Sauval, A. J. 1998, Space Sci. Rev., 85, 161
Guilloteau, S., Omont, A., McMahon, R. G., Cox, P., & Petitjean, P. 1997, A&A, 328, L1
Haardt, F., & Madau, P. 1996, ApJ, 461, 20
Haiman, Z., Rees, M. J., & Loeb, A. 1997, ApJ, 476, 458
Henry, R. B. C., Edmunds, M. G., & Köppen, J. 2000, ApJ, 541, 660
Henry, R. B. C., & Worthey, G. 1999, PASP, 111, 919
Hollenbach, D. J., Werner, M. W., & Salpeter, E. E. 1971, ApJ, 163, 165
Howk, J. C., Sembach, K. R., Roth, K. C., & Kurk, J. W. 2000, ApJ, 544, 867
Israelian, G., Rebolo, R., García López, R. J., Bonifacio, P., Molaro, P., Basri, G., & Shchukina, N. 2001, ApJ, 551, 833
Iwata, I., Ohta, K., Nakanishi, K., Kohno, K., & McMahon, R. G. 2001, PASJ, 53, 871
Jenkins, E. B., & Peimbert, A. 1997, ApJ, 477, 265
Jenkins, E. B., Woźniak, P. R., Sofia, U. J., Sonneborn, G., & Tripp, T. M. 2000, ApJ, 538, 275
Jura, M. 1974, ApJ, 191, 375
———. 1975a, ApJ, 197, 575
———. 1975b, ApJ, 197, 581
Kunth, D., Lequeux, J., Sargent, W. L. W., & Viallefond, F. 1994, A&A, 282, 709
Launay, J. M., & Roueff, E. 1977a, A&A, 56, 289
———. 1977b, J. Phys. B, 10, 879
Ledoux, C., Petitjean, P., Bergeron, J., Wampler, E. J., & Srianand, R. 1998, A&A, 337, 51
Levshakov, S. A., Agafonova, I. I., & Kegel, W. H. 2000a, A&A, 360, 833
Levshakov, S. A., Chaffee, F. H., Foltz, C. B., & Black, J. H. 1992, A&A, 262, 385
Levshakov, S. A., & Foltz, C. B. 1988, Soviet Astron. Lett., 14, 467
Levshakov, S. A., Foltz, C. B., Chaffee, F. H., & Black, J. H. 1989, AJ, 98, 2052
Levshakov, S. A., Kegel, W. H., & Takahara, F. 1998, ApJ, 499, L1
———. 1999a, MNRAS, 302, 707
Levshakov, S. A., Molaro, P., Centurión, M., D'Odorico, S., Bonifacio, P., & Vladilo, G. 2000b, A&A, 361, 803
———. 2001, in ESO/ST-ECF/STScI Conf. Proc., Deep Fields, in press

Levshakov, S. A., Takahara, F., & Agafonova, I. I. 1999b, ApJ, 517, 609
Levshakov, S. A., Tytler, D., & Burles, S. 2000c, Astron. Astrophys. Trans., 19, 385
Levshakov, S. A., & Varshalovich, D. A. 1985, MNRAS, 212, 517
Linsky, J. L. 1998, Space Sci. Rev., 84, 285
Lopez, S., Reimers, D., Rauch, M., Sargent, W. L. W., & Smette, A. 1999, ApJ, 513, 598
Lu, L., Sargent, W. L. W., Barlow, T. A., Churchill, C. W., & Vogt, S. S. 1996, ApJS, 107, 475
Mather, J. C., Fixsen, D. J., Shafer, R. A., Mosier, C., & Wilkinson, D. T. 1999, ApJ, 512, 511
Mathis, J. S., Mezger, P. G., & Panagia, N. 1983, A&A, 128, 212
Meyer, D. M., Lanzetta, K. M., & Wolfe, A. M. 1995, ApJ, 451, L13
Meyer, D. M., & York, D. G. 1992, ApJ, 399, L121
Meyer, S. L. 1975, Data Analysis for Scientists and Engineers (New York: Wiley)
Molaro, P., Bonifacio, P., Centurión, M., D'Odorico, S., Vladilo, G., Santin, P., & Di Marcantonio, P. 2000, ApJ, 541, 54
Molaro, P., Levshakov, S. A., Dessauges-Zavadsky, M., & D'Odorico, S. 2001a, A&A, in press
Molaro, P., Levshakov, S. A., D'Odorico, S., Bonifacio, P., & Centurión, M. 2001b, ApJ, 549, 90
Møller, P., & Warren, S. J. 1993, A&A, 270, 43
Moos, H. W., et al. 2000, ApJ, 538, L1
Morton, D. C. 1991, ApJS, 77, 119
Morton, D. C., & Dinerstein, H. L. 1976, ApJ, 204, 1
Netterfield, C. B., et al. 2001, ApJ, submitted (astro-ph/0104460)
Nishimura, S. 1968, Ann. Tokyo Astron. Obs., 11, 33
Ohta, K., Yamada, T., Nakanishi, K., Kokno, K., Akiyama, M., & Kawabe, R. 1996, Nature, 382, 426
Omont, A., Petitjean, P., Guilloteau, S., McMahon, R. G., Solomon, P. M., & Pecontal, E. 1996, Nature, 382, 428
Osmer, P. S., & Smith, M. G. 1980, ApJS, 42, 333
Outram, P. J., Chaffee, F. H., & Carswell, R. F. 1999, MNRAS, 310, 289
Papadopoulos, P. P., Ivison, R., Carilli, C., & Lewis, G. 2001, Nature, 409, 58
Papadopoulos, P. P., Röttgering, H. J. A., van der Werf, P. P., Guilloteau, S., Omont, A., van Breugel, W. J. M., & Tilanus, R. P. J. 2000, ApJ, 528, 626
Petitjean, P., Srianand, R., & Ledoux, C. 2000, A&A, 364, L26
Pettini, M., Ellison, S. L. Steidel, C. C., & Bowen, D. V. 1999, ApJ, 510, 576
Pettini, M., Ellison, S. L., Steidel, C. C., Shapley, A. E., & Bowen, D. V. 2000, ApJ, 532, 65
Pettini, M., Smith, L. J., Hunstead, R. W., & King, D. L. 1994, ApJ, 426, 79
Pierre, M., Shaver, P. A., & Robertson, J. G. 1990, A&A, 235, 15
Press, W. H., Teukolsky, S. A., Vetterling, W. T., & Flannery, B. P. 1992, Numerical Recipes (Cambridge: Cambridge Univ. Press)
Prochaska, J. X., & Wolfe, A. 1999, ApJS, 121, 369
Raassen, A. J. J., & Uylings, P. H. M. 1998, J. Phys. B, 31, 3137
Richter, P., et al. 1998, A&A, 338, L9
Savage, B. D., Drake, J. F., Budich, W., & Bohlin, R. C. 1977, ApJ, 216, 291
Shull, J. M., & Beckwith, S. 1982, ARA&A, 20, 163
Shull, J. M., et al. 2000, ApJ, 538, L73
Silva, A. I., & Viegas, S. M. 2001, MNRAS, in press
Sofia, V. J., & Jenkins, E. B. 1998, ApJ, 499, 951
Solomon, P. M., Downes, D., & Radfort, S. J. E. 1992, ApJ, 398, L29
Spitzer, L., Jr., & Cochran, W. D. 1973, ApJ, 186, L23
Spitzer, L., Jr., Cochran, W. D., & Hirshfeld, A. 1974, ApJS, 28, 373
Spitzer, L., Jr., & Fitzpatrick, E. L. 1993, ApJ, 409, 299
Spitzer, L., Jr., & Jenkins, E. B. 1975, ARA&A, 13, 133
Spitzer, L., Jr., & Morton, W. A. 1976, ApJ, 204, 731
Spitzer, L., Jr., & Zweibel, E. G. 1974, ApJ, 191, L127
Srianand, R., & Petitjean, P. 1998, A&A, 335, 33
Srianand, R., Petitjean, P., & Ledoux, C. 2000, Nature, 408, 931
Tikhonov, A. N., & Arsenin, V. A. 1977, Solution of Ill-Posed Problems (Washington, DC: Winston & Sons)
Turner, J., Kirby-Docken, K., & Dalgarno, A. 1977, ApJS, 35, 281
Tytler, D., O'Meara, J. M., Suzuki, N., & Lubin, D. 2000, Phys. Rep., 333, 409
Vidal-Madjar, A., et al. 2000, ApJ, 538, L77
Vladilo, G. 1998, ApJ, 493, 583
Vladilo, G., Bonifacio, P., Centurión, M., & Molaro, P. 2000, ApJ, 543, 24
Williger, G. M., Carswell, R. F., Webb, J. K., Boksenberg, A., & Smith, M. G. 1989, MNRAS, 237, 635
Wolfe, A. M., & Briggs, F. H. 1981, ApJ, 248, 460
Wolfe, A. M., et al. 1994, ApJ, 435, L101
Wolfe, A. M., Lanzetta, K. M., Foltz, C. B., & Chaffee, F. H. 1995, ApJ, 454, 698